Said, Mokhtar; Shaheen, Abdullah M.; Ginidi, Ahmed R.; El-Sehiemy, Ragab A.; Mahmoud, Karar; Lehtonen, Matti; Darwish, Mohamed M. F.

Estimating Parameters of Photovoltaic Models Using Accurate Turbulent Flow of Water Optimizer

Published in:
Processes

DOI:
10.3390/pr9040627

Published: 02/04/2021

Document Version
Publisher's PDF, also known as Version of record

processes

MDPI

Article

Estimating Parameters of Photovoltaic Models Using Accurate Turbulent Flow of Water Optimizer

Mokhtar Said [1], Abdullah M. Shaheen [2], Ahmed R. Ginidi [2], Ragab A. El-Sehiemy [3], Karar Mahmoud [4,5], Matti Lehtonen [4] and Mohamed M. F. Darwish [4,6,*]

[1] Department of Electrical Engineering, Faculty of Engineering, Fayoum University, 43518 Fayoum, Egypt; msi01@fayoum.edu.eg
[2] Department of Electrical Engineering, Faculty of Engineering, Suez University, 41522 Suez, Egypt; abdullah.mohamed.eng19@suezuni.edu.eg (A.M.S.); ahmed.ginidi@eng.suezuni.edu.eg (A.R.G.)
[3] Department of Electrical Engineering, Faculty of Engineering, Kafrelshiekh University, 33516 Kafrelshiekh, Egypt; elsehiemy@eng.kfs.edu.eg
[4] Department of Electrical Engineering and Automation, School of Electrical Engineering, Aalto University, FI-00076 Espoo, Finland; karar.mostafa@aalto.fi (K.M.); matti.lehtonen@aalto.fi (M.L.)
[5] Department of Electrical Engineering, Faculty of Engineering, Aswan University, 81542 Aswan, Egypt
[6] Department of Electrical Engineering, Faculty of Engineering at Shoubra, Benha University, 11629 Cairo, Egypt
* Correspondence: mohamed.m.darwish@aalto.fi or mohamed.darwish@feng.bu.edu.eg

Citation: Said, M.; Shaheen, A.M.; Ginidi, A.R.; El-Sehiemy, R.A.; Mahmoud, K.; Lehtonen, M.; Darwish, M.M.F. Estimating Parameters of Photovoltaic Models Using Accurate Turbulent Flow of Water Optimizer. *Processes* **2021**, *9*, 627. https://doi.org/10.3390/pr9040627

Academic Editor: Masoud Soroush

Received: 2 March 2021
Accepted: 29 March 2021
Published: 2 April 2021

Abstract: Recently, the use of diverse renewable energy resources has been intensively expanding due to their technical and environmental benefits. One of the important issues in the modeling and simulation of renewable energy resources is the extraction of the unknown parameters in photovoltaic models. In this regard, the parameters of three models of photovoltaic (PV) cells are extracted in this paper with a new optimization method called turbulent flow of water-based optimization (TFWO). The applications of the proposed TFWO algorithm for extracting the optimal values of the parameters for various PV models are implemented on the real data of a 55 mm diameter commercial R.T.C. France solar cell and experimental data of a KC200GT module. Further, an assessment study is employed to show the capability of the proposed TFWO algorithm compared with several recent optimization techniques such as the marine predators algorithm (MPA), equilibrium optimization (EO), and manta ray foraging optimization (MRFO). For a fair performance evaluation, the comparative study is carried out with the same dataset and the same computation burden for the different optimization algorithms. Statistical analysis is also used to analyze the performance of the proposed TFWO against the other optimization algorithms. The findings show a high closeness between the estimated power–voltage (P–V) and current–voltage (I–V) curves achieved by the proposed TFWO compared with the experimental data as well as the competitive optimization algorithms, thanks to the effectiveness of the developed TFWO solution mechanism.

Keywords: photovoltaic; parameter extraction; TFWO; optimization; double diode model; and three diode model

1. Introduction

Human life is stable and immovable due to energy. The development and progress of energy are necessary for a better life. The conventional sources of energy are depleted and cause environmental exacerbation, so the dependence on energy from renewable energy sources is inevitable as they are clean, have no environmental problems, exist in large quantities and provide energy with high capability [1–5]. One of the most important renewable energy sources is solar energy, where solar irradiation can be transformed effectively into electrical energy via photovoltaic (PV) cells/modules and may directly supply electric loads or be stored in batteries or other storage devices [6,7].

Several advanced applications have been introduced based on PV electricity, such as feeding the required power for satellite communication [8], greenhouse cooling and heating [9], water pumping for agriculture [10–12], supplying electronic devices and indoor lighting [13,14], etc. The PV characteristics can be analyzed with power–voltage (P–V) and current–voltage (I–V) curves. These curves are dependent on several parameters, such as incident solar irradiance, ambient temperature, and the investigated equivalent circuit of the PV model [15–18]. The PV characteristics depend on different unknown parameters due to a lack of data from the PV manufacturing datasheet [19]. Improving and analyzing the performance of PV cells/modules is imperative due to their widespread applications, which require optimal extraction of the unknown parameters. These parameters are changed according to the investigated PV models which can be a single diode model (SDM), double diode model (DDM), and three diode model (TDM). Consequently, the number of unknown parameters are five, seven and nine for the SDM, DDM, and TDM, respectively.

These parameters are estimated in three ways: iterative methods, machine learning, and meta-heuristic optimization algorithms [20–26]. The iterative methods have been applied to estimate the PV parameters in [27–30], such as Lambert W function [27], linear least squares [28], maximum likelihood-based Newton–Raphson [29], and Gauss–Seidel [30]. On the other hand, several researchers made an assumption or neglected some parameters to reduce the number of variables required to be extracted.

Lately, various optimization techniques have been carried out in the extraction of PV parameters, such as the elephant herd algorithm [31], multiple learning backtracking search algorithm [32], gray wolf optimizer, cuckoo search algorithm [33], opposition-based sine cosine approach with local search [34], logistic chaotic JAYA algorithm [35], moth–flame algorithm (MFA), orthogonal Nelder–Mead MFA [36], and improved teaching–learning-based optimization (TBLO) algorithm [37]. In [38], the MFA has been utilized for the three diode PV model considering the ideality factors for the second and third diode as added control variables. In [39], these parameters have been estimated with an interval branch and bound global optimization algorithm. In [40], simplified TBLO has been applied to estimate the parameters in a TDM. In addition, parameter extraction has been prepared by an improved version of the whale optimization algorithm [41] and chaotic improved artificial bee colony (CIABC) [42]. There is no doubt that the accuracy of the behavior of PVs is based on the estimated parameters, so the optimization techniques need further development to achieve high accuracy of these parameters. Additionally, in [43], another optimization method called forensic optimizer was developed for finding the optimal parameters of various solar cells. In [44], the gradient based optimizer was developed for three diode models.

As seen in the literature, incredible work has been performed in the extraction of the optimal PV model parameters. A global solution has not been accomplished as the randomization process is a property of all optimization search algorithms. Among of the previous optimization methods, a new optimization method called turbulent flow of water-based optimization (TFWO) [45] is developed for finding the parameters of three models of PV cells. Several new optimization techniques, such as the marine predators algorithm (MPA), equilibrium optimization (EO), and manta ray foraging optimization (MRFO), are used to compare the results of the proposed algorithm with the same dataset. Statistical analysis is used to analyze the performance of the proposed optimization algorithm. The P–V and I–V curves are simulated for the value of the estimated parameter that makes the simulated data very close to the experimental data.

The organization of this paper is as follows: Section 2 explains the analysis of the objective function to be handled in the problem formulation. Section 3 contains the details of the proposed TFWO algorithm. Section 4 analyzes the results of the studied cases, while the conclusion is drawn in Section 5.

2. Problem Formulation and Objective Function

Three models of PVs are analyzed in this section, SDM, DDM, and TDM [44], to be formulated in the objective function.

2.1. Analysis of SDM

Figure 1 explains the SDM equivalent circuit of the PV solar cell. The mathematical equations to calculate the output current of the SDM can be formulated as follows:

$$I = I_{ph} - I_{d1} - I_{sh} \tag{1}$$

$$I = I_{ph} - I_{s1}\left[e^{\frac{q(V+IR_s)}{a_1 KT_c}} - 1\right] - \frac{V + IR_s}{R_{sh}} \tag{2}$$

where I is the current output from the solar cell SDM, I_{ph} is the photogenerated current, I_{sh} is the current due to leakage in the PN junction, I_{d1} is the dark saturation current of the SDM, R_{sh} is the shunt resistance, R_s is the series resistance, a_1 is the diode ideality factor, K is Boltzmann's constant, q is the charge of the electron, and T_c is the cell temperature.

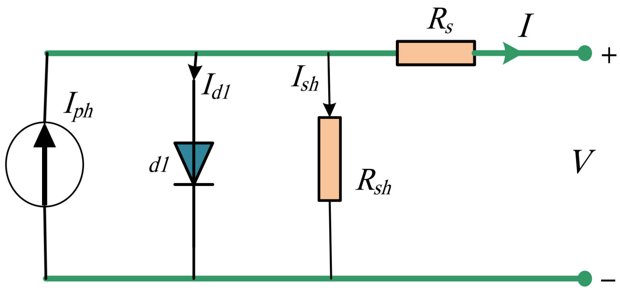

Figure 1. Single diode model (SDM) equivalent circuit.

According to the previous mathematical formula, the five unknown parameters required to estimate the SDM are $\left(I_{ph},\ I_{s1},\ a_1,\ R_s,\ R_{sh}\right)$.

2.2. Analysis of DDM

Figure 2 explains the DDM equivalent circuit of the PV solar cell. The mathematical equations to compute the output current of the DDM are as follows:

$$I = I_{ph} - I_{d1} - I_{d2} - I_{sh} \tag{3}$$

$$I = I_{ph} - I_{s1}\left[e^{\frac{q(V+IR_s)}{a_1 KT_c}} - 1\right] - I_{s2}\left[e^{\frac{q(V+IR_s)}{a_2 KT_c}} - 1\right] - \frac{V + IR_s}{R_{sh}} \tag{4}$$

where I_{d2} is the dark saturation current of the second diode in the DDM, a_2 is the ideality factor of the second diode. In this model, seven parameters should be estimated, which are $\left(I_{ph},\ I_{s1},\ a_1,\ R_s,\ R_{sh},\ I_{s2},\ a_2\right)$.

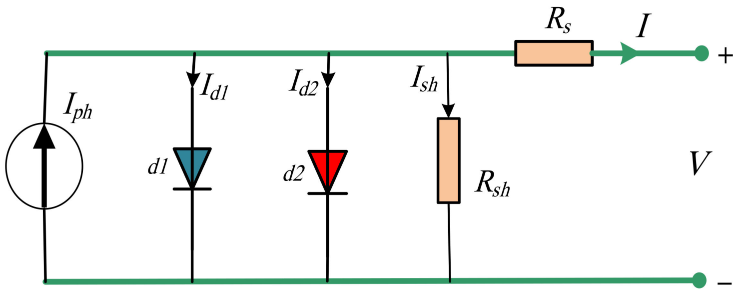

Figure 2. Double diode model (DDM) equivalent circuit.

2.3. Analysis of TDM

Figure 3 illustrates the TDM equivalent circuit related to the PV solar cell. The mathematical equations to compute the output current of the TDM are as follows:

$$I = I_{ph} - I_{d1} - I_{d2} - I_{d3} - I_{sh} \tag{5}$$

$$I = I_{ph} - I_{s1}\left[e^{\frac{q(V+IR_s)}{a_1 KT_c}} - 1\right] - I_{s2}\left[e^{\frac{q(V+IR_s)}{a_2 KT_c}} - 1\right] - I_{s3}\left[e^{\frac{q(V+IR_s)}{a_3 KT_c}} - 1\right] - \frac{V+IR_s}{R_{sh}} \tag{6}$$

where I_{d3} is the dark saturation current of the third diode in the TDM, a_3 is the ideality factor of the third diode. In this model, nine parameters should be estimated, which are $\left(I_{ph},\ I_{s1},\ a_1,\ R_s\ ,\ R_{sh}\ ,\ I_{s2}\ ,\ a_2\ ,\ I_{s3}\ ,\ a_3\right)$.

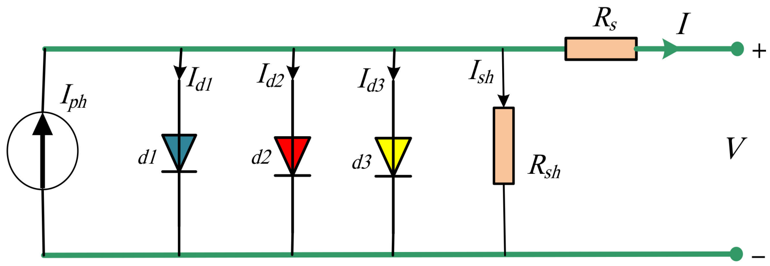

Figure 3. Three diode model (TDM) equivalent circuit.

2.4. Estimated Objective Function

Minimizing the root mean square error (*RMSE*) of the PV characteristics between the estimated parameters and the experimental results is an important objective function to be considered. Therefore, the decision variables (X) are extracted in each run of the optimizer. The mathematical formula to compute *RMSE* can be formulated as follows:

$$RMSE = \sqrt{\frac{1}{N}\sum_{i=1}^{N}(J(V,I,X)^2} \tag{7}$$

$$J(V,I,X) = I - I_{\text{exp}} \tag{8}$$

where I_{exp} is the experimental current, N is the reading data number, V is the experimental voltage, I is the estimated current, and X is the decision variables that are calculated as follows:

For SDM, $X = \left\{\left(I_{ph},\ I_{s1},\ a_1,\ R_s\ ,\ R_{sh}\ \right)\right\}$.

For DDM, $X = \left\{\left(I_{ph},\ I_{s1},\ a_1,\ R_s\ ,\ R_{sh}\ ,\ I_{s2}\ ,\ a_2\ \right)\right\}$.

For TDM, $X = \left\{\left(I_{ph},\ I_{s1},\ a_1,\ R_s\ , R_{sh}\ ,\ I_{s2}\ ,\ a_2\ ,\ I_{s3}\ ,\ a_3\right)\right\}$.

3. Proposed Turbulent Flow of Water-Based Optimization Algorithm

The turbulent flow of water-based optimization algorithm (TFWOA), which was presented by Mojtaba Ghasemi et al. [45], is inspired by the principle of irregular fluctuations of water turbulent flow. In this type of turbulent flow, the magnitude and direction speed are continuously changing in a circular form. Then, the water flows downwards in a spiral path. In this algorithm, a whirlpool represents a random behavior of nature that can occur in seas, oceans or rivers. The center of the whirlpool is considered a sucking hole, and it pulls the particles across it towards the middle. To illustrate, the whirlpool uses centripetal force on them, which involves a volume of moving water created by the ocean tide. Centripetal force is characterized as a force that is employed in a circular path on a moving object, and its direction is in the direction of the center of the motion pathway of the object and perpendicular to it. The centripetal force shifts the moving pathway of the object without changing the velocity. Firstly, the initial population of the algorithm (N_p members) (comprising X^0) is split into an equal rate between N_{wh} groups which represent the whirlpool sets. Secondly, the strongest member of each whirlpool set (the member with better objective function values) $f(X)$ is considered as the whirlpool that pulls the objects.

Every whirlpool (Wh) behaves as a sucking well and has a tendency to unify the locations of objects inside its set (X) with its central position through applying a centripetal force on them and pushing them into its well. Thus, the jth whirlpool and the local position on $W\ h_j$ combines the ith object position (X_i) with itself ($X_i = Wh_j$). However, other whirlpools produce some deviations (ΔX_i) because of the distance between them ($Wh - Wh_j$) and their objective values ($f(X)$) as well. Accordingly, the new position of the ith object becomes $X_i^{new} = Wh_j - \Delta X_i$.. and the objects ($X$) move with their special angle (δ) across their whirlpool's center and move toward it. Hence, this angle in each iteration is changing according to Equation (9):

$$\delta_i^{new} = \delta_i + r_1 * r_2 * \pi \tag{9}$$

To model and calculate the farthest and nearest whirlpools (ΔX_i), Equation (10) depicts the whirlpools with the least weighed distance from all objects, and then ΔX_i is calculated using Equation (11). Equation (12) is used to update the position of the particle.

$$\Delta_t = f(Wh_t) * |Wh_t - sum(X_i)|^{0.5} \tag{10}$$

$$\begin{aligned} \Delta X_i = {} & (\cos(\delta_i^{new}) * r(1, D) * (Wh_f - X_i) \\ & - \sin(\delta_i^{new}) * r(1, D) * (Wh_w - X_i)) * \\ & (1 + \left|\cos(\delta_i^{new}) - \sin(\delta_i^{new})\right|) \end{aligned} \tag{11}$$

$$X_i^{new} = Wh_j - \Delta X_i \tag{12}$$

where Wh_f and Wh_w manifest the whirlpools with the minimum and maximum of Δ_t, respectively, while δ_i characterizes the ith object's angle.

Centrifugal force (FE_i) sometimes overcomes the centripetal force of the whirlpool and randomly transfers the object to a new location. The centrifugal force is modeled as illustrated in Equation (13), which randomly occurs in one dimension of the decision variables. To attain this, the centrifugal force is calculated according to the angle between the whirlpool and object, as manifested in Equation (13), and if this force is greater than a random value in the range [0,1], the centrifugal action is performed for a randomly selected dimension, as shown in Equation (14). This phenomenon is formulated mathematically as:

$$FE_i = \left((\cos(\delta_i^{new}))^2 * (\sin(\delta_i^{new}))^2\right)^2 \tag{13}$$

$$X_{i,p} = X_p^{\min} - r * (X_p^{\max} - X_p^{\min}) \tag{14}$$

The whirlpools interact with and displace each other. This phenomenon can be modeled in the same way as the impacts of whirlpools on the objects, where every whirlpool has a tendency to pull other whirlpools and apply the centripetal force on them. The nearest whirlpool can be mathematically represented based on the minimum amount and its objective function, as illustrated in Equation (15). Then, the whirlpool's position can be updated according to Equations (16) and (17).

$$\Delta_t = f(Wh_t) * \left|Wh_t - sum(Wh_j)\right|^{0.5} \tag{15}$$

$$\begin{aligned} \Delta Wh_j = {} & r(1, D) * \left|\cos(\delta_j^{new}) + \sin(\delta_j^{new})\right| \\ & *(Wh_f - Wh_j) \end{aligned} \tag{16}$$

$$\Delta Wh_j^{new} = Wh_f - Wh_j \tag{17}$$

where δ_j represents the jth whirlpool hole angle value.

Eventually, when the strongest member has more strength among the new members of the whirlpool set, which means that the value of the objective function is less than its corresponding whirlpool, it is chosen as a new whirlpool for the next iteration. The flowchart of the TFWOA is depicted in Figure 4.

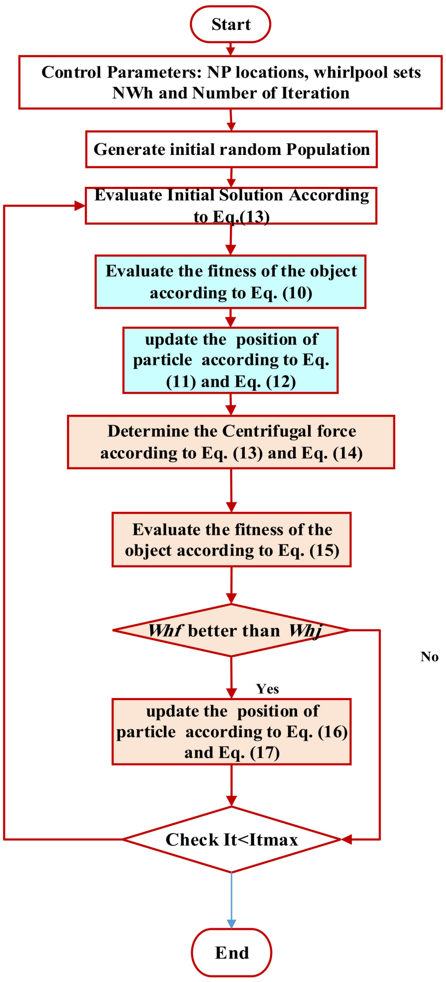

Figure 4. Flowchart of the turbulent flow of water-based optimization algorithm (TFWOA).

4. Simulation Results and Discussion

This section presents the application and analysis of the proposed TFWO algorithm for extracting the optimal values of the parameters of various PV models. Real data of a 55 mm diameter commercial R.T.C. France solar cell [7,44] and experimental data of a KC200GT module [46] are considered. The considered boundaries of the parameters are explained in Table 1.

Table 1. The extracted parameters boundaries of test solar cells and modules.

	R.T.C. France Solar Cell [7]		KC200GT Module [7]	
Parameters	**Lower Bound**	**Upper Bound**	**Lower Bound**	**Upper Bound**
I_{ph}	0	1	0	9
$I_{s1} \,.\, I_{s2} \,.\, I_{s3}$ (µA)	0	1	0	1
R_s	0	0.5	0	0.5
R_{sh}	0	100	0	100
$a_1 \,.\, a_2 \,.\, a_3$	1	2	1	2

4.1. Compared Algorithms

Several optimization algorithms are employed and compared to the proposed TFWO (Turbulent Flow of Water Optimizer) for the same purpose. These algorithms are the backtracking search optimization algorithm (BSA) [47], gray wolf optimizer (GWO) [48], crow search optimization algorithm (CSO) [49], equilibrium optimizer (EO) [50], marine predators algorithm (MPA) [51], Bernstein–Levy search differential evolution algorithm (BSDE) [52] and manta ray foraging optimization (MRFO) [53]. The BSA, GWO and CSO have different successive applications, while the EO, MPA, BSDE, and MRFO are very recent algorithms from 2020. Table 2 represents examples of their recent applications.

Table 2. Several recent applications of the compared algorithms.

Algorithm	Published Year	Recent Applications
BSA [47]	2013	Reconfiguration in distribution networks (2020) [54], reactive power dispatch (2018) [55], parameter optimization of the support vector machine (2020) [56].
GWO [48]	2014	Coordination of VAR compensators and distributed energy resources (2020) [57], allocation of distributed generation in power systems (2020) [58], energy management, and battery size optimization (2020) [59].
CSO [49]	2016	Short-term wind speed forecasting (2020) [60], capacitor allocation in distribution networks (2017) [61], emission economic dispatch [62]
EO [50]	2020	Multi-thresholding image segmentation problems [63], operation of hybrid AC/DC grids (2020) [64].
MPA [51]	2020	Large-scale photovoltaic array reconfiguration (2020) [65], task scheduling in IoT-based fog computing applications (2020) [66].
BSDE [52]	2021	Not applicable yet.
MRFO [53]	2020	Fuel cell exergy analysis (2020) [67], optimal power flow (2020) [68], maximum power point (2020) [69].
TFWO [45]	2021	Not applicable yet.

All these algorithms have the merit of utilizing adaptive internal control parameters. For all algorithms, the population size is specified as 100, where the maximum number of iterations is taken as 1000 and 2000 for an R.T.C. France solar cell and KC200GT module, respectively. The compared algorithms in Table 3 are employed for optimal extraction of the PV parameters with the SDM, DDM, and TDM. The convergence performance, robustness, and accuracy for all algorithms used in this work are found based on 30 separate runs for each algorithm.

Table 3. The parameters extracted for R.T.C. France SDM at the best root mean square error (*RMSE*).

Algorithm	I_{ph} (A)	I_{d1} (A)	a_1	R_s (Ω)	R_{sh} (Ω)	*RMSE*
TFWO	0.760775529	3.23×10^{-7}	1.481183723	0.036377085	53.71858096	0.000986022
MRFO	0.760778817	3.22884×10^{-7}	1.481141648	0.036380748	53.67819867	0.000986034
BSDE	0.760773529	3.23008×10^{-7}	1.481179386	0.036378015	53.74364455	0.000986023
MPA	0.760846832	3.22991×10^{-7}	1.48119268	0.036361364	52.76698061	0.000987369
EO	0.76077794	3.22162×10^{-7}	1.480915424	0.036387935	53.64156933	0.000986035
CSO	0.760757142	3.24211×10^{-7}	1.481546607	0.036366384	54.0990705	0.000986181
GWO	0.760695583	3.58429×10^{-7}	1.491737687	0.035974121	57.26269608	0.001008231
BSA	0.760850914	3.11696×10^{-7}	1.477614787	0.036510097	51.96067738	0.000989471

4.2. Statistical Analysis for R.T.C. France Solar Cell

4.2.1. Single Diode Model

Table 3 provides the optimal values of the control variables related to the best run for the compared algorithms. As shown, TFWO obtains the minimum *RMSE* of 0.000986022 compared to the others. Based on TFWO, the photo-generated current is 0.760775529 A; the dark saturation current of the SDM is 0.323 µA; the diode ideality factor is 1.481183723; the series resistance is 0.036377085 Ω; the shunt resistance is 53.71858096 Ω. Figure 5 describes the convergence rates of the algorithms and shows that the capability of the proposed TFWO in finding the minimum *RMSE* is the fastest.

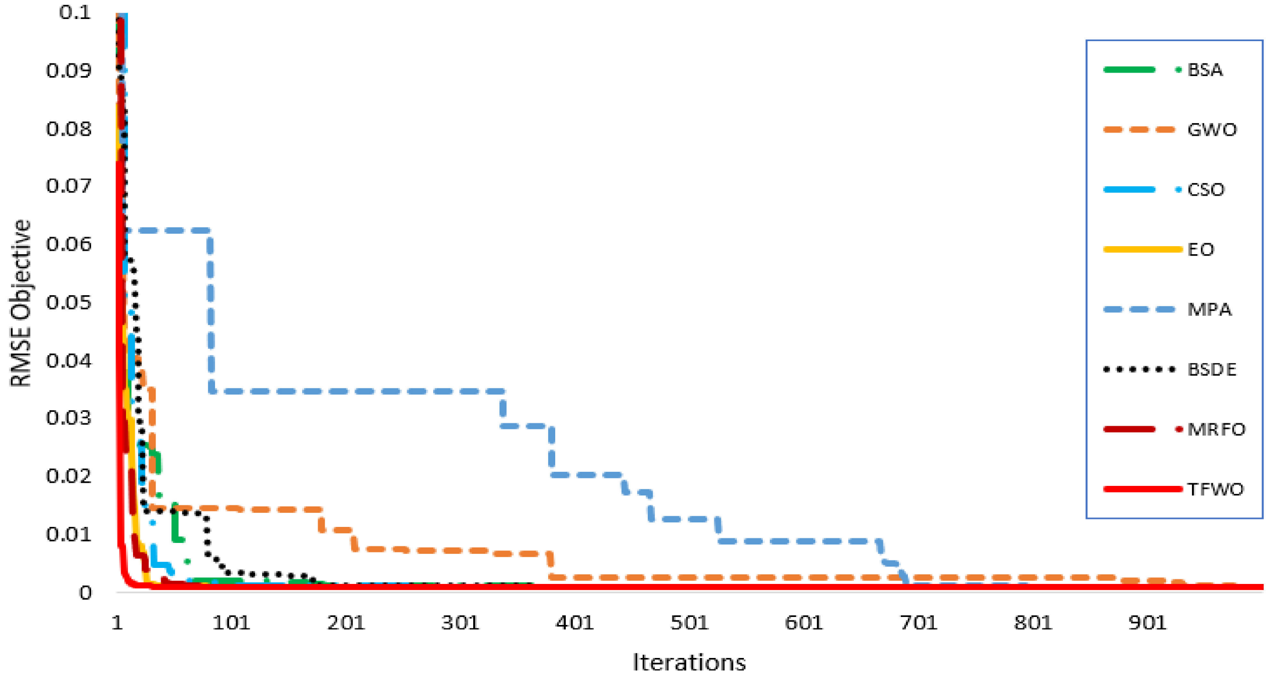

Figure 5. Convergence curves for R.T.C. France SDM.

Based on the extracted PV parameters using the TFWO, Figure 6 describes the I–V and P–V characteristic curves in comparison to the experimental data. This figure illustrates the great similarity between the extracted curves based on TFWO and the experimental results. Figure 7 shows this capability, where the error for each value of current and power is shown between the simulated and experimental data to measure the quality of the result.

Table 4 records the minimum, maximum, mean, and standard deviation of the *RMSE* for the SDM. This table declares that TFWO presents the highest robustness characteristics. It gives the lowest values of the minimum, maximum, mean, and standard deviation of the *RMSE*, at 0.000986022, 0.000986205, 0.00098603, and 3.35307×10^{-8}, respectively. Meanwhile, the second-best *RMSE* (0.000986023) is achieved by the BSDE, followed by MRFO, EO, CSO, MPA, BSA, and GWO. Figure 8 displays the RMS values of the 30 runs for the R.T.C. France SDM. This figure shows the significant robustness feature of the proposed TFWO since all the acquired values of the *RMSE* based on TFWO are the lowest values compared with the other methods.

Table 4. Statistical analysis of *RMSE* for R.T.C. France SDM.

Algorithm	*RMSE*			
	Min.	**Max.**	**Mean**	**SD**
TFWO	0.00098602	0.00098620	0.00098603	3.353×10^{-8}
MRFO	0.00098603	0.00105788	0.00100505	2.143×10^{-5}
BSDE	0.00098602	0.00103025	0.00099520	1.056×10^{-5}
MPA	0.00098736	0.00481175	0.00217485	0.00065237
EO	0.00098603	0.00105604	0.00100209	1.783×10^{-5}
CSO	0.00098618	0.00130296	0.00105888	8.095×10^{-5}
GWO	0.00100823	0.03816637	0.00637283	0.0112567
BSA	0.000989471	0.001161862	0.001037488	4.42885×10^{-5}

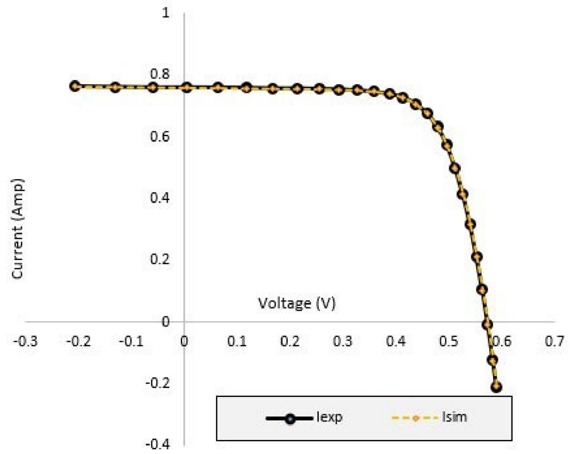

(**a**)

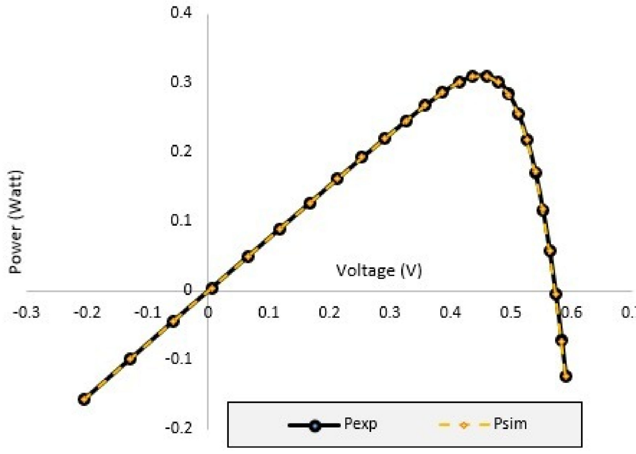

(**b**)

Figure 6. Characteristic curves for R.T.C. France SDM based on parameters extracted from TFWO: (**a**) Current–voltage (I–V) ch/s and (**b**) power–voltage (P–V) ch/s.

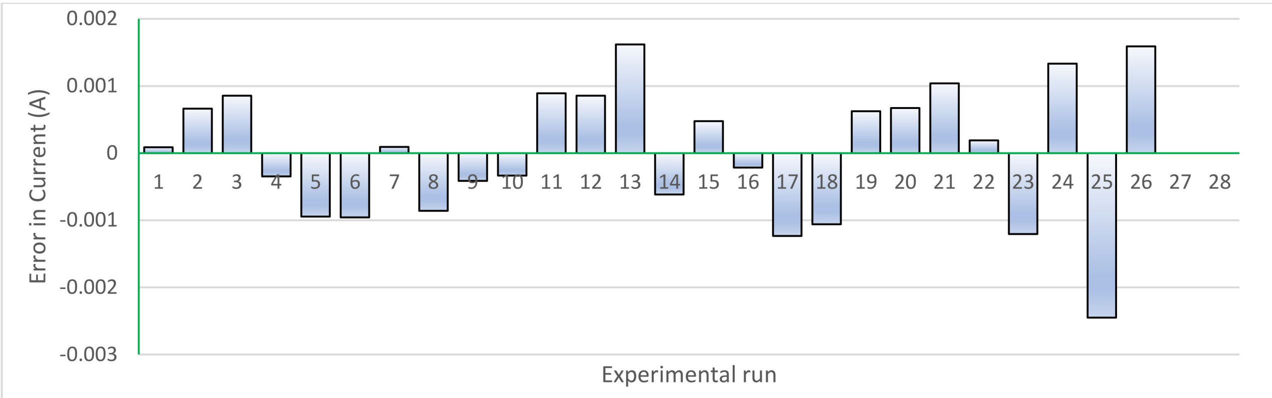

(**a**)

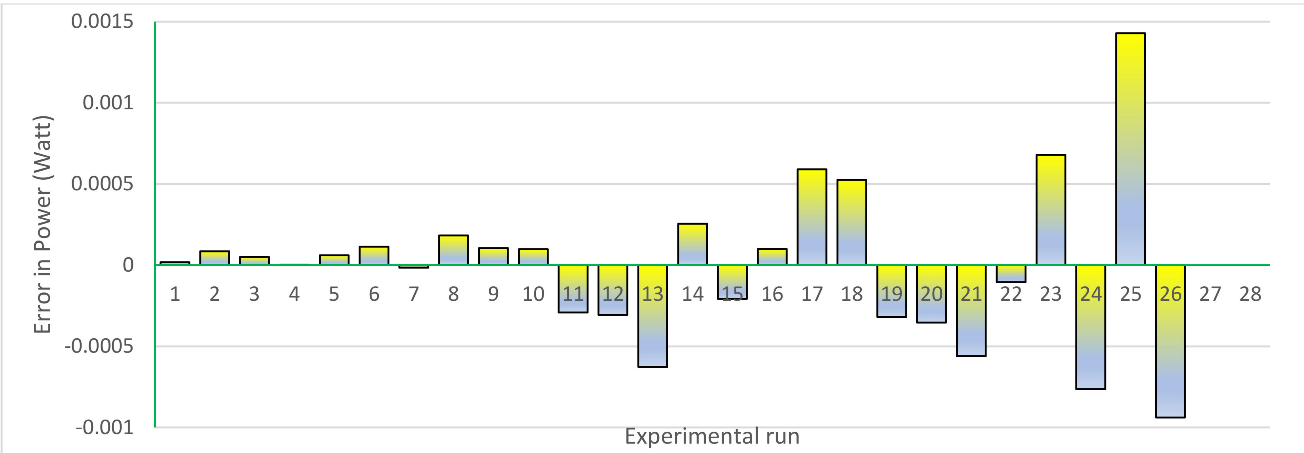

(**b**)

Figure 7. Error values for R.T.C. France SDM based on parameters extracted from TFWO: (**a**) Current error values and (**b**) power error values.

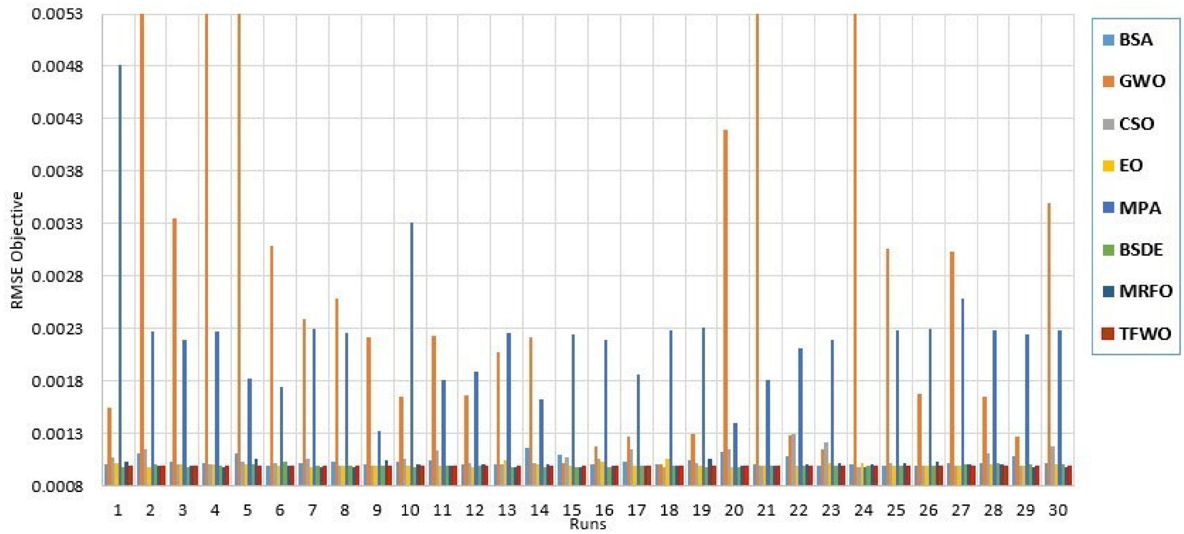

Figure 8. The RMS values of the 30 runs for R.T.C. France SDM.

4.2.2. Double Diode Model

The proposed TFWO and the compared algorithms are applied for this model. Table 5 provides the optimal values of the control variables related to the best run, while Figure 9 describes their convergence rates. From both, it can be observed that the best *RMSE* value (0.000982723) is achieved by the TFWO algorithm, while the second-best *RMSE* (0.000983378) is achieved by MRFO, followed by CSO, EO, BSDE, BSA, GWO, and MPA.

Table 5. The parameters extracted for R.T.C. France DDM.

Algorithm	I_{ph} (A)	R_s (Ω)	R_{sh} (Ω)	*RMSE*	I_{d1} (A)	a_1	I_{d2} (A)	a_2
TFWO	0.760782016	0.036839463	55.91920478	0.000982723	2.06×10^{-7}	1.443289469	9.24×10^{-7}	2
MRFO	0.760743575	0.036597626	54.95169271	0.000983378	4.37429×10^{-7}	1.998364786	2.62887×10^{-7}	1.463671024
BSDE	0.760782257	0.036991096	54.62889674	0.000989247	1.38431×10^{-7}	1.416972632	5.71114×10^{-7}	1.764756216
MPA	0.760918727	0.037865706	53.18011281	0.001026823	7.66125×10^{-8}	1.36857525	9.99997×10^{-7}	1.815337209
EO	0.760741801	0.036329661	54.62831228	0.000986861	3.06281×10^{-7}	1.492418793	2.85646×10^{-8}	1.428995768
CSO	0.760756875	0.03652498	54.63222775	0.000983888	3.22867×10^{-7}	1.992580518	2.7755×10^{-7}	1.46831668
GWO	0.760583028	0.036533827	58.81767959	0.001003603	3.2814×10^{-7}	1.563347542	8.25411×10^{-8}	1.41082037
BSA	0.760980002	0.036723119	53.23192348	0.000993668	2.64414×10^{-7}	1.705891588	1.99393×10^{-7}	1.446025602

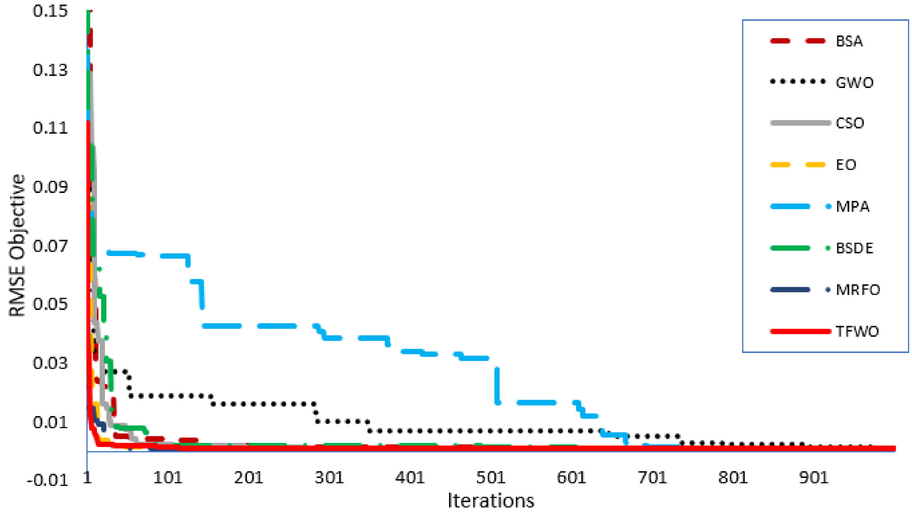

Figure 9. The convergence curves for R.T.C. France DDM.

Based on the extracted PV parameters using the TFWO, Figure 10 describes the I–V and P–V characteristic curves in comparison to the experimental data, while Figure 11 displays the related errors. From both figures, the coincidence of the simulated data based on TFWO with the experimental data is very high.

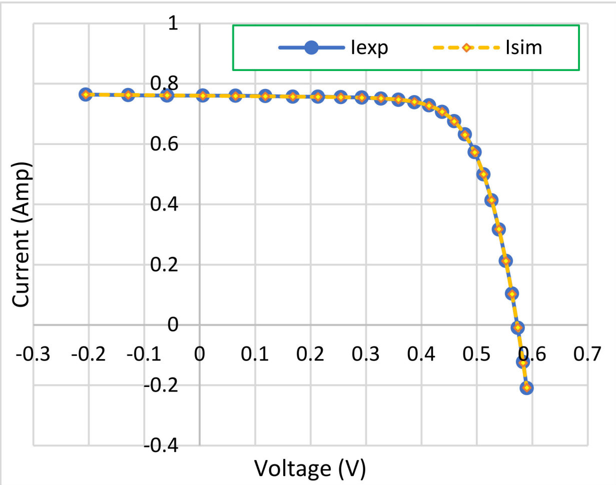

(**a**)

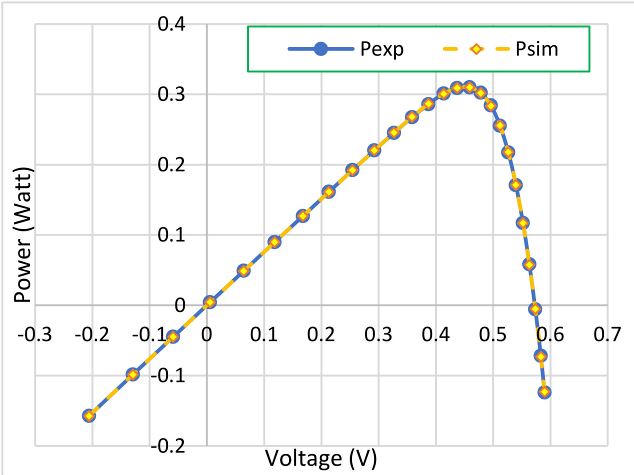

(**b**)

Figure 10. Characteristic curves for R.T.C. France DDM based on TFWO: (**a**) I–V ch/s and (**b**) P–V ch/s.

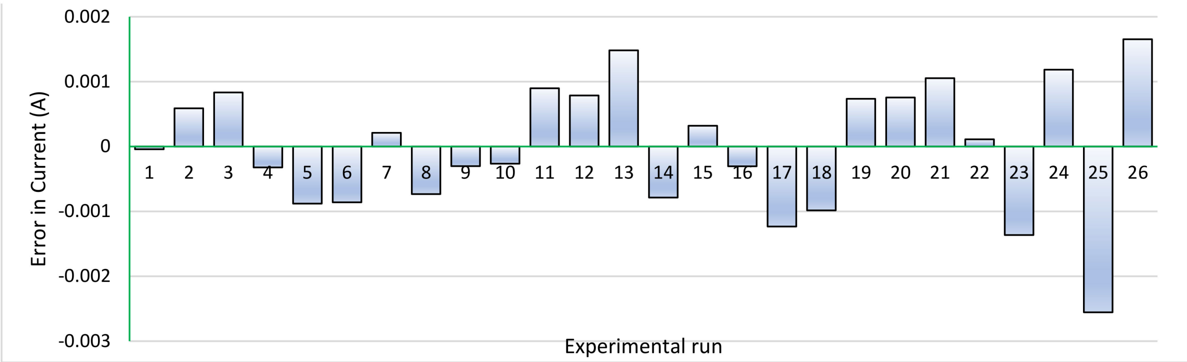

(**a**)

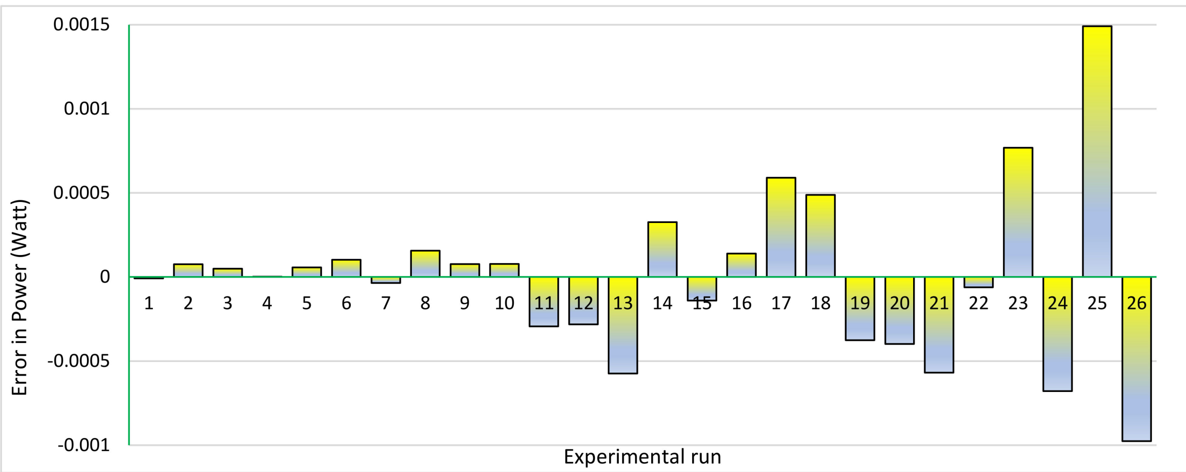

(**b**)

Figure 11. Error values for R.T.C. France DDM based on TFWO: (**a**) Current error values and (**b**) power error values.

Table 6 records the minimum, maximum, mean, and standard deviation of the *RMSE* for the DDM. This table declares that TFWO presents the highest robustness characteristics. It gives the lowest values of the minimum, maximum, mean, and standard deviation of the *RMSE* as 0.000982723, 0.0012, 0.00099392, and 3.9352×10^{-5}, respectively. Figure 12 displays the *RMSE* values of the 30 runs for the R.T.C. France DDM. The acquired values of the *RMSE* based on the proposed TFWO are lower than their comparable values based on the others.

Table 6. Statistical analysis of *RMSE* for R.T.C. France DDM.

Algorithm	*RMSE*			
	Min.	**Max.**	**Mean**	**SD**
TFWO	0.000982723	0.0012	0.00099392	3.9352×10^{-5}
MRFO	0.000983378	0.001353061	0.001077661	8.45223×10^{-5}
BSDE	0.000989247	0.001492072	0.001113348	0.000112212
MPA	0.001026823	0.002869201	0.001779704	0.000616954
EO	0.000986861	0.001256857	0.001033158	6.33746×10^{-5}
CSO	0.000983888	0.001428127	0.00113901	0.000155378
GWO	0.001003603	0.038150899	0.00640054	0.011254562
BSA	0.000993668	0.001214824	0.001080621	5.45125×10^{-5}

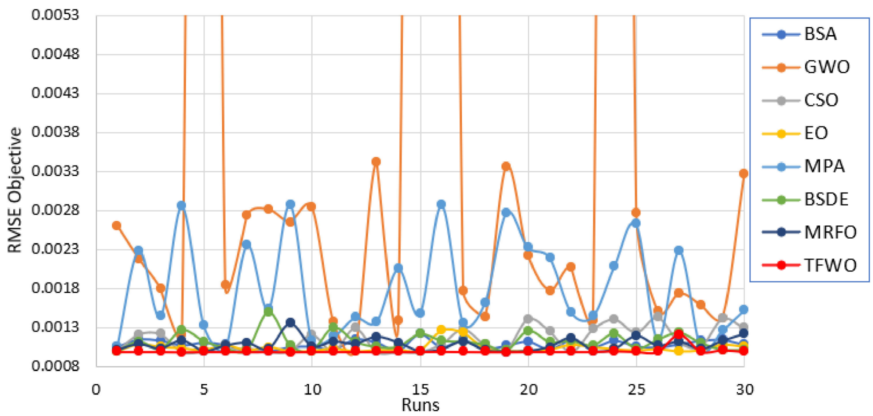

Figure 12. The RMS values of the 30 runs for R.T.C. France DDM.

4.2.3. Three Diode Model

For this model, Table 7 provides the optimal values of the control variables related to the best run of the proposed TFWO and the compared algorithms, while Figure 13 describes their convergence rates. From both, it can be observed that the best *RMSE* value (0.000983646) is achieved by the TFWO algorithm, while the second-best *RMSE* (0.000984242) is achieved by CSO, followed by MRFO, EO, BSA, MPA, BSDE, and GWO. Figure 14 describes the I–V and P–V characteristic curves in comparison with the experimental data, while Figure 15 displays the related errors. From both figures, the coincidence of the simulated data based on TFWO with the experimental data is very high.

Table 7. The parameters extracted for R.T.C. France TDM.

Algorithm	BSA	GWO	CSO	EO	MPA	BSDE	MRFO	TFWO
I_{ph} (A)	0.76088788	0.761840018	0.760767839	0.760733925	0.760665312	0.76060128	0.760721516	0.7608
I_{s1} (A)	6.11525×10^{-8}	6.26386×10^{-7}	8.65078×10^{-7}	2.29078×10^{-7}	2.60174×10^{-15}	1.33125×10^{-7}	2.6918×10^{-7}	0
a_1	1.665282347	1.972178035	1.992247826	1.945636832	1.025249938	1.715044852	1.880941278	1
R_s (Ω)	0.036740001	0.036238306	0.036859716	0.036427424	0.037130986	0.036693181	0.036566016	0.0367
R_{sh} (Ω)	53.18712346	43.25339883	54.98736983	55.52914763	59.57973022	60.17938354	55.20751535	55.2261
I_{s2} (A)	8.13561×10^{-8}	7.69448×10^{-9}	4.64418×10^{-11}	9.51489×10^{-8}	6.85783×10^{-7}	2.119×10^{-7}	7.27156×10^{-8}	2.39243×10^{-7}
a_2	1.951596911	1.982906016	1.583874031	1.981076476	1.670531807	1.449412901	1.755268871	1.4558
I_{s3} (A)	2.62168×10^{-7}	2.41707×10^{-7}	2.06159×10^{-7}	2.78562×10^{-7}	4.54209×10^{-8}	4.27168×10^{-7}	2.41083×10^{-7}	6.38605×10^{-7}
a_3	1.464894557	1.457809556	1.443266003	1.469223538	1.348012837	1.942277098	1.458171437	2
RMSE	0.001002321	0.001293402	0.000984242	0.000985451	0.001002377	0.001029117	0.000984843	0.000983646

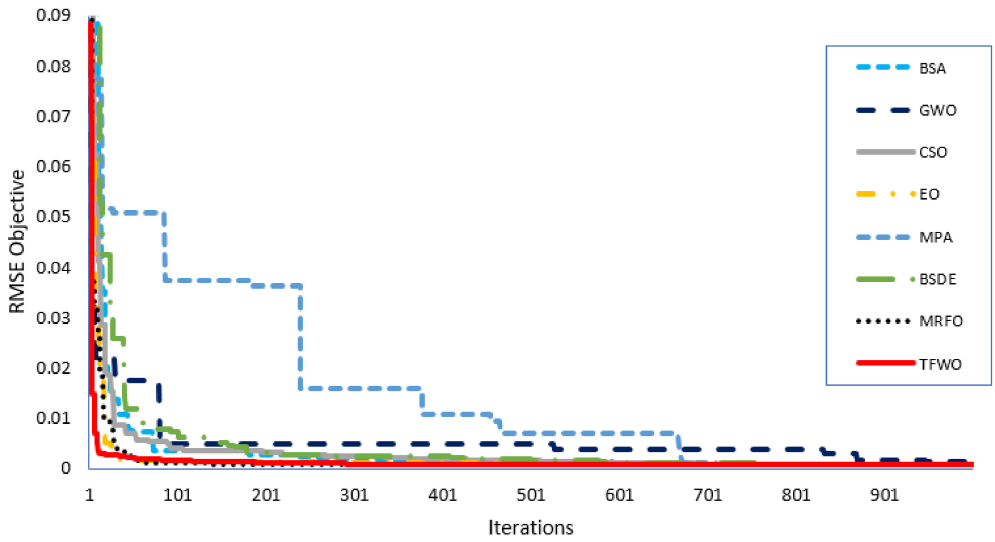

Figure 13. The convergence curves for R.T.C. France TDM.

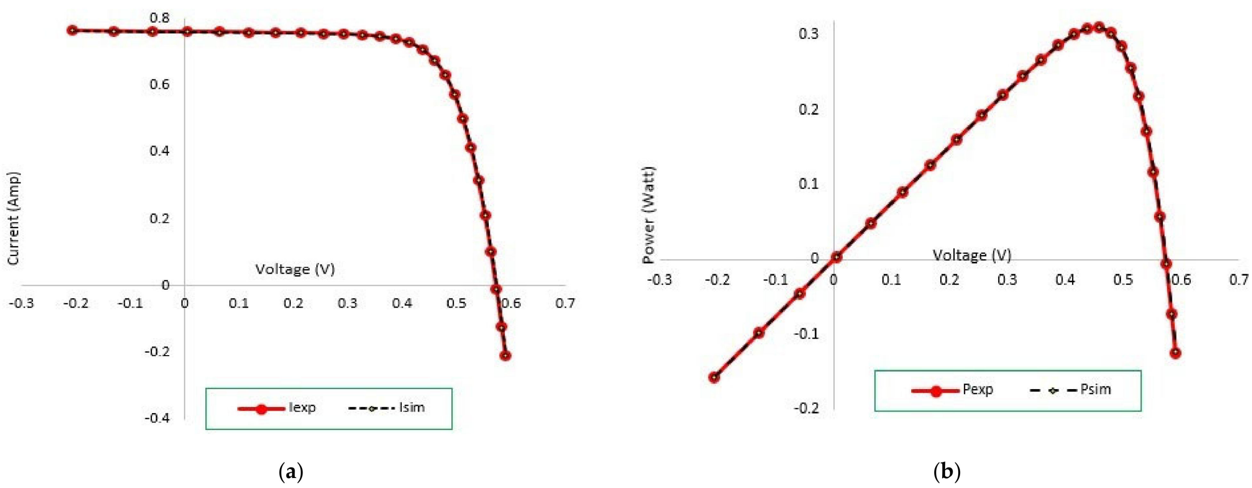

Figure 14. Characteristic curves for R.T.C. France TDM based on TFWO: (**a**) I–V ch/s and (**b**) P–V ch/s.

For the 30 runs, the minimum, maximum, mean, and standard deviation of the *RMSE* are tabulated in Table 8. As shown, the proposed TFWO gives the lowest values of the minimum, maximum, mean, and standard deviation as 0.000983646, 0.00102314, 0.000987683, and 7.32713×10^{-6}, respectively. Figure 16 displays the *RMSE* values of the 30 runs for the R.T.C. France TDM, which demonstrate the efficacy of the proposed TFWO in finding the minimum *RMSE* values compared to the others.

Table 8. Statistical analysis of *RMSE* for R.T.C. France TDM.

Algorithm	*RMSE*			
	Min.	**Max.**	**Mean**	**SD**
TFWO	0.000983646	0.00102314	0.000987683	7.32713×10^{-6}
MRFO	0.000984843	0.001492643	0.001164256	0.000129441
BSDE	0.001029117	0.002051955	0.001320873	0.000243075
MPA	0.001002377	0.005305369	0.002200116	0.000900812
EO	0.000985451	0.001393105	0.001131243	0.00011292
CSO	0.000984242	0.00191729	0.001164341	0.000184491
GWO	0.001293402	0.033393772	0.006435657	0.01033541
BSA	0.001002321	0.001567976	0.001189651	0.000119982

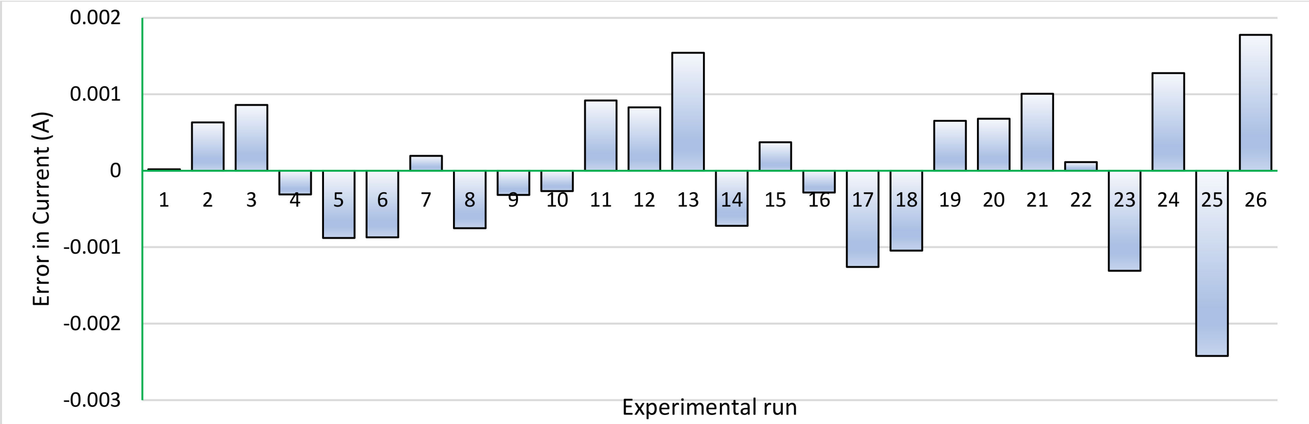

(a)

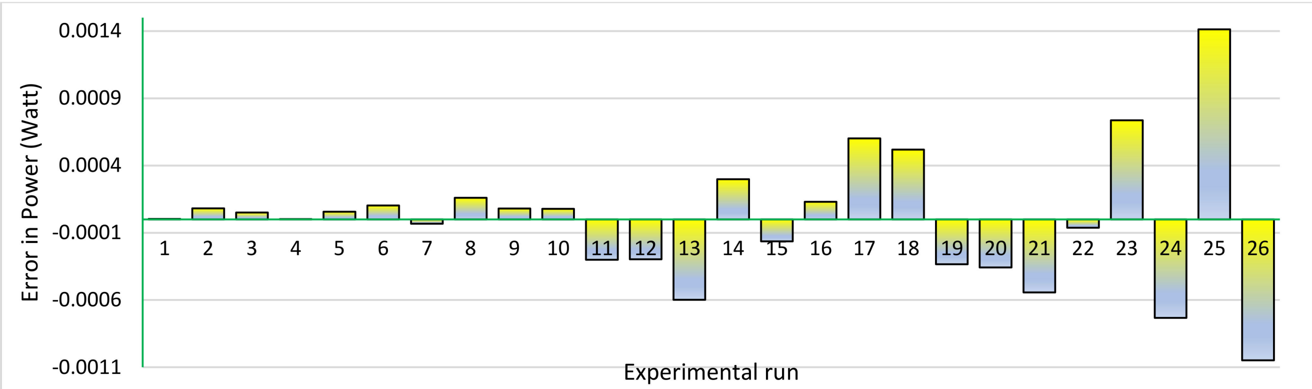

(b)

Figure 15. Error values for R.T.C. France TDM based on TFWO: (**a**) Current error values and (**b**) power error values.

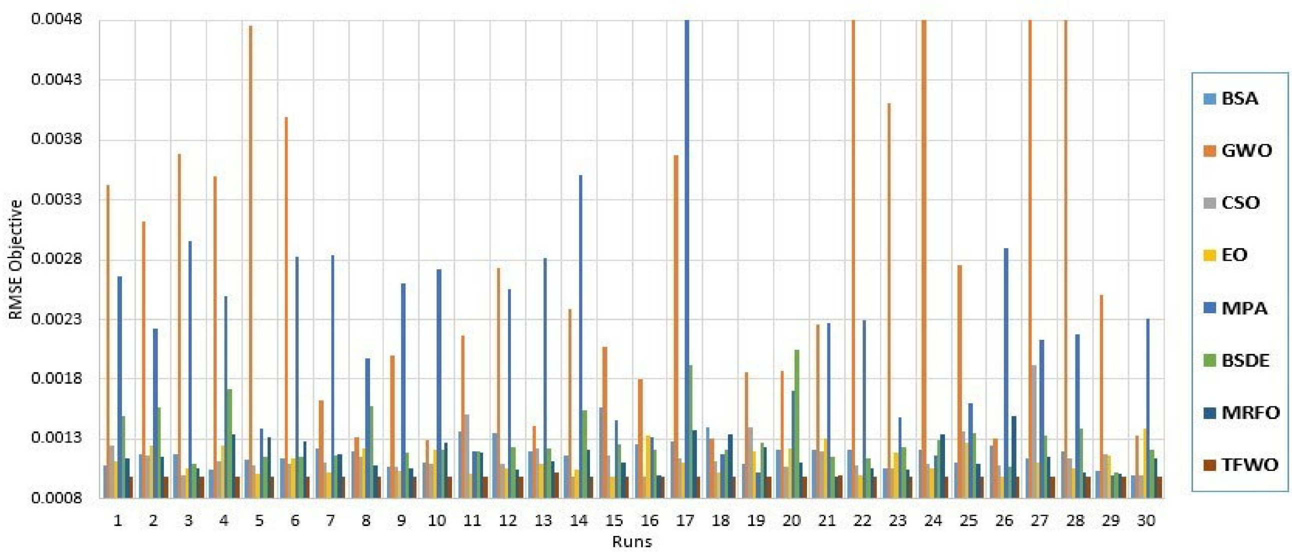

Figure 16. The RMS values of the 30 runs for R.T.C. France TDM.

4.3. Statistical Analysis for KC200GT Solar Module

4.3.1. Single Diode Model

The comparison of the results for the SDM is explained in Table 9; this table includes the best *RMSE* and the parameters extracted from each algorithm. From Table 9, it can be observed that the best *RMSE* value (0.000636657) is achieved by the TFWO algorithm, while the second-best *RMSE* (0.002888472) is achieved by EO, followed by MRFO, BSDE, BSA, MPA, CSO, and GWO. Based on TFWO, the photo-generated current is 8.216747428 A; the dark saturation current of the SDM is 0.0262486 μA; the diode ideality factor is 1.212957711; the series resistance is 0.004825464 Ω; the shunt resistance is 6.284632281 Ω. Figure 17 describes the convergence rates of the algorithms which show that the capability of the proposed TFWO in finding the minimum *RMSE* is the fastest. Added to that, the P–V and I–V curves for the SDM based on the estimated data from TFWO at the best *RMSE* are explained in Figure 18, which illustrates the high coincidence of the simulated with the experimental data.

Table 9. Extracted parameters for KC200GT SDM.

Algorithm	I_{ph} (A)	I_{s1} (A)	a_1	R_s (Ω)	R_{sh} (Ω)	*RMSE*
TFWO	8.216747428	2.62486×10^{-8}	1.212957711	0.004825464	6.284632281	0.000636657
MRFO	8.212405132	3.36662×10^{-8}	1.228520397	0.004754881	7.037075568	0.003374264
BSDE	8.210553583	3.43101×10^{-8}	1.229705769	0.004756865	7.555908952	0.003467884
MPA	8.184927	7.94459×10^{-8}	1.285180059	0.004537611	92.14823504	0.0148696
EO	8.209152899	2.85259×10^{-8}	1.218067754	0.004814539	7.714703106	0.002888472
CSO	8.188955905	8.18358×10^{-8}	1.287282057	0.004540479	87.91105559	0.015480743
GWO	8.193721562	1.72203×10^{-7}	1.341187392	0.004264421	84.34172349	0.023476598
BSA	8.187828492	4.39672×10^{-8}	1.245523356	0.004706406	17.16016059	0.009775873

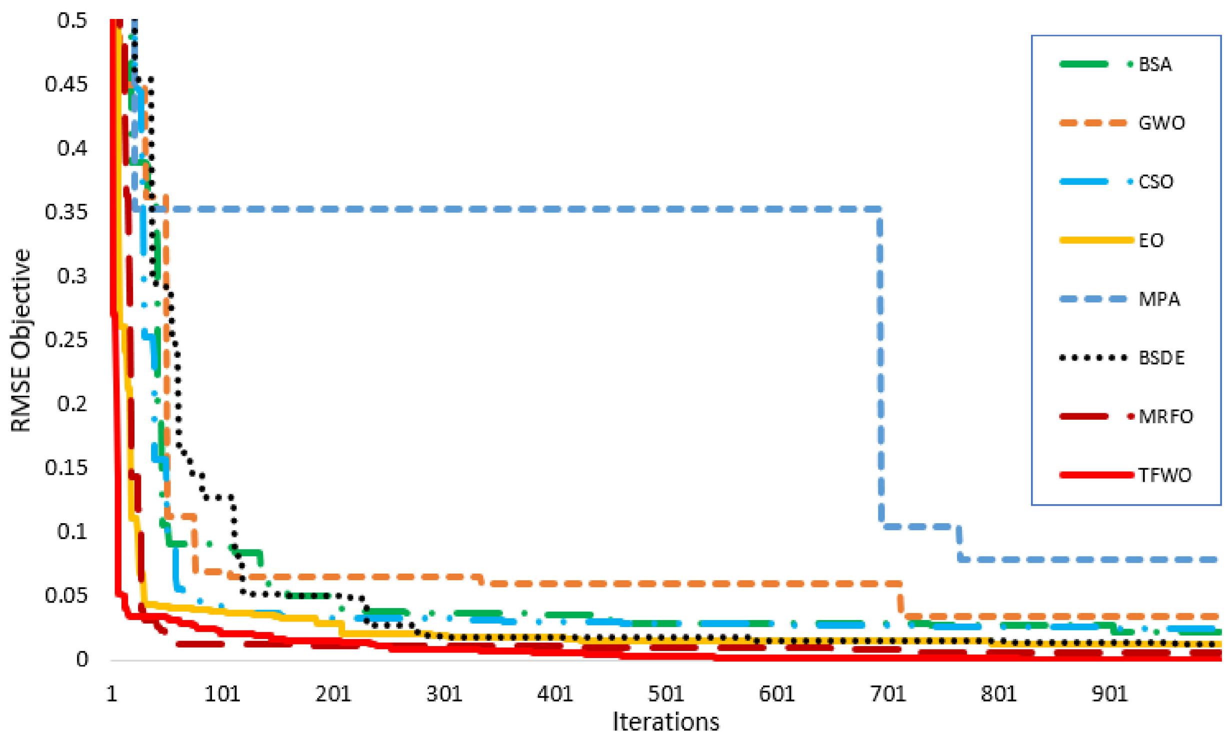

Figure 17. The convergence curves for KC200GT SDM.

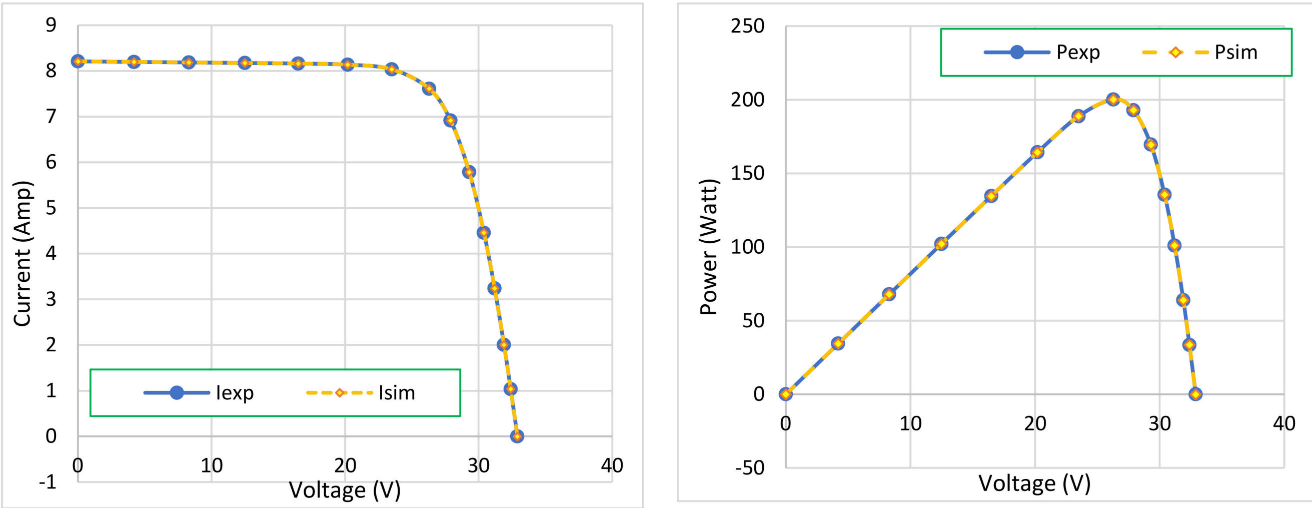

(a) (b)

Figure 18. Characteristic curves for KC200GT SDM based on TFWO: (**a**) I–V ch/s and (**b**) P–V ch/s.

4.3.2. Double Diode Model

For this model, Table 10 shows the optimal values of the control variables related to the best run of the compared algorithms, while Figure 19 illustrates their convergence rates. From both, it can be observed that the best *RMSE* value (0.000464919) is achieved by the TFWO algorithm, while the second-best *RMSE* (0.002599915) is achieved by EO, followed by CSO, MRFO, GWO, BSA, BSDE, and MPA. Figure 20 describes the I–V and P–V characteristic curves in comparison to the experimental data.

Table 10. Extracted parameters for KC200GT DDM.

Algorithm	I_{ph} (A)	R_s (Ω)	R_{sh} (Ω)	I_{s1} (A)	a_1	I_{s2} (A)	a_2	*RMSE*
TFWO	8.215931265	0.00490447	6.55275986	9.75×10^{-11}	1	4.58×10^{-8}	1.266697565	0.000464919
MRFO	8.207554293	0.004729	7.962198358	1.30925×10^{-7}	1.956231371	3.89385×10^{-8}	1.237993335	0.008229492
BSDE	8.199742079	0.004618981	11.00371597	1.70333×10^{-7}	1.898851719	5.22564×10^{-8}	1.257319714	0.009849963
MPA	8.184775806	0.005037849	96.10264033	8.62345×10^{-7}	1.581206361	4.01866×10^{-10}	1.017081239	0.01025436
EO	8.210884382	0.004777302	7.422135219	9.02611×10^{-9}	1.822712307	3.13628×10^{-8}	1.224039636	0.002599915
CSO	8.204148086	0.004890878	9.331329018	7.23319×10^{-8}	1.304927843	1.27128×10^{-10}	1.000421712	0.004212996
GWO	8.188942442	0.004865207	20.87443954	7.54227×10^{-7}	1.765240036	1.56333×10^{-8}	1.185224915	0.009625309
BSA	8.204090314	0.004601853	10.29800978	5.53×10^{-8}	1.260653585	3.03837×10^{-8}	1.998785758	0.009625725

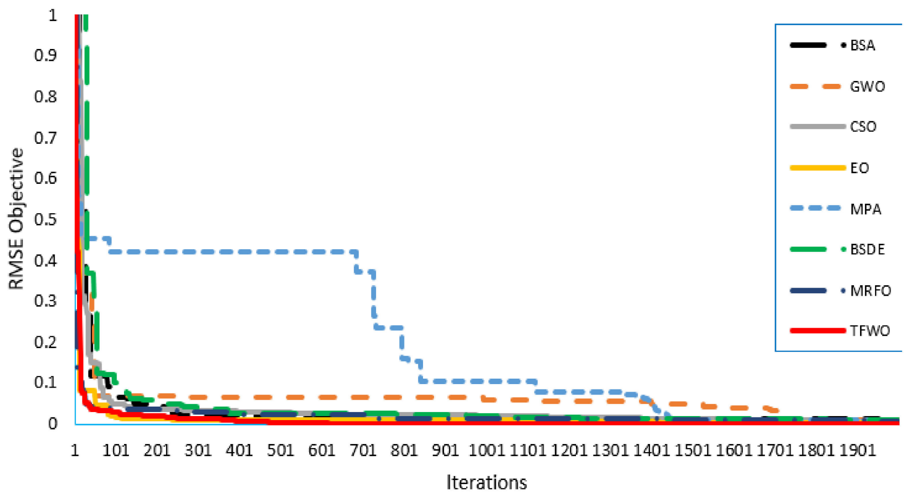

Figure 19. The convergence curves for KC200GT DDM.

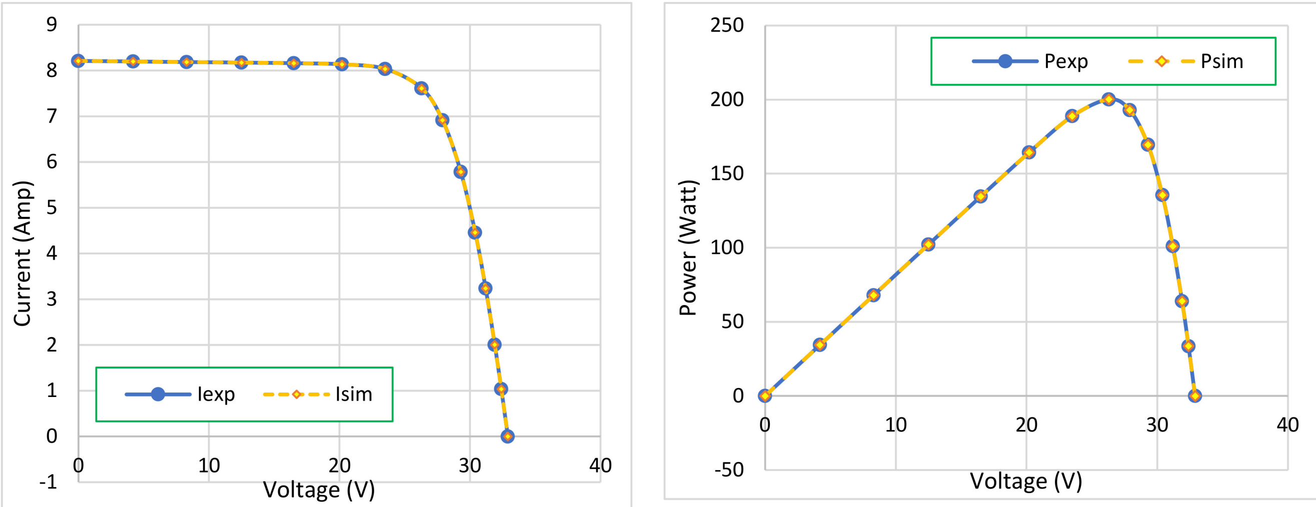

(**a**) (**b**)

Figure 20. Characteristic curves for KC200GT DDM based on TFWO: (**a**) I–V ch/s and (**b**) P–V ch/s.

4.3.3. Three Diode Model

For this model, Table 11 and Figure 21 show the optimal values of the control variables of the compared algorithms and their convergence rates, respectively. From both, the best *RMSE* value (0.000379678) is achieved by the proposed TFWO. The P–V and I–V curves for the TDM based on the estimated data from TFWO at the best *RMSE* are explained in Figure 22, whilst the error for each value of current and power between the simulated and experimental data is found to measure the quality of the result, as shown in Figure 23. From both, the coincidence of the simulated data based on TFWO with the experimental data is very high.

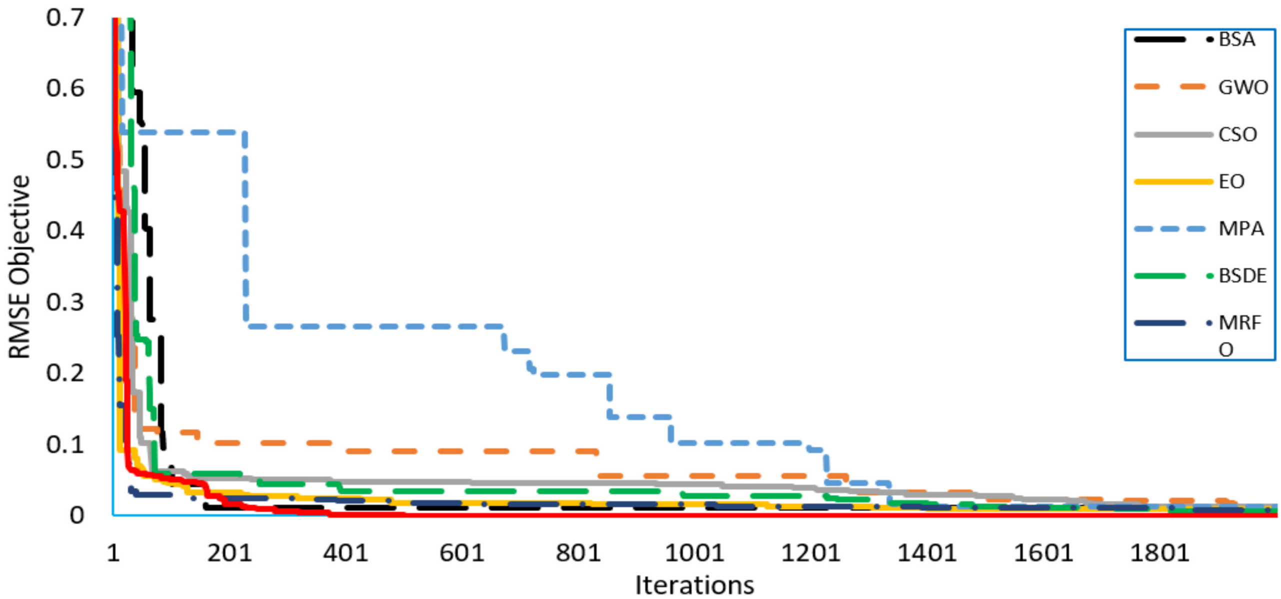

Figure 21. The convergence curves for KC200GT TDM.

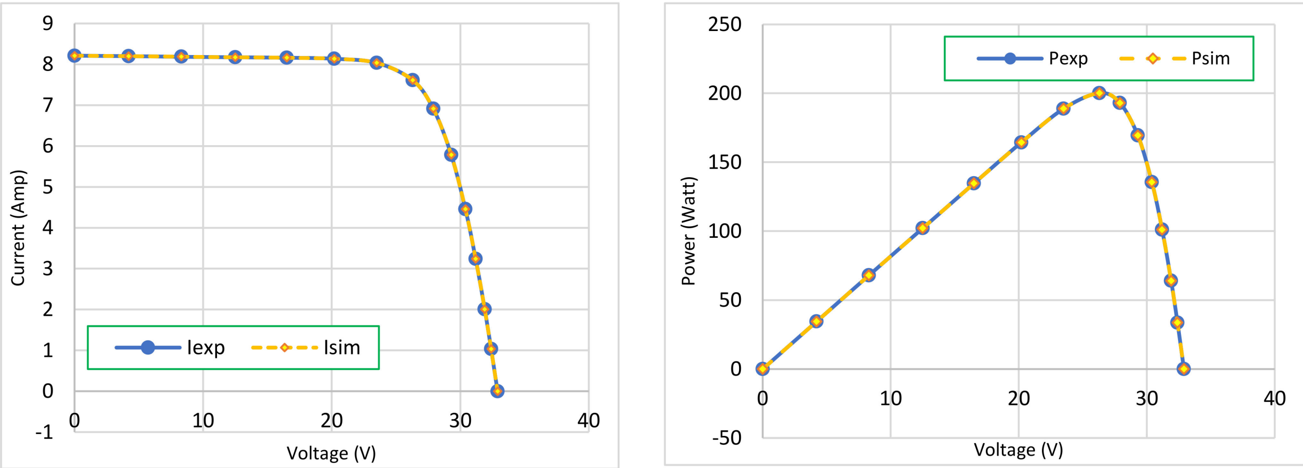

(a) (b)

Figure 22. Characteristic curves for KC200GT TDM based on TFWO: (**a**) I–V ch/s and (**b**) P–V ch/s.

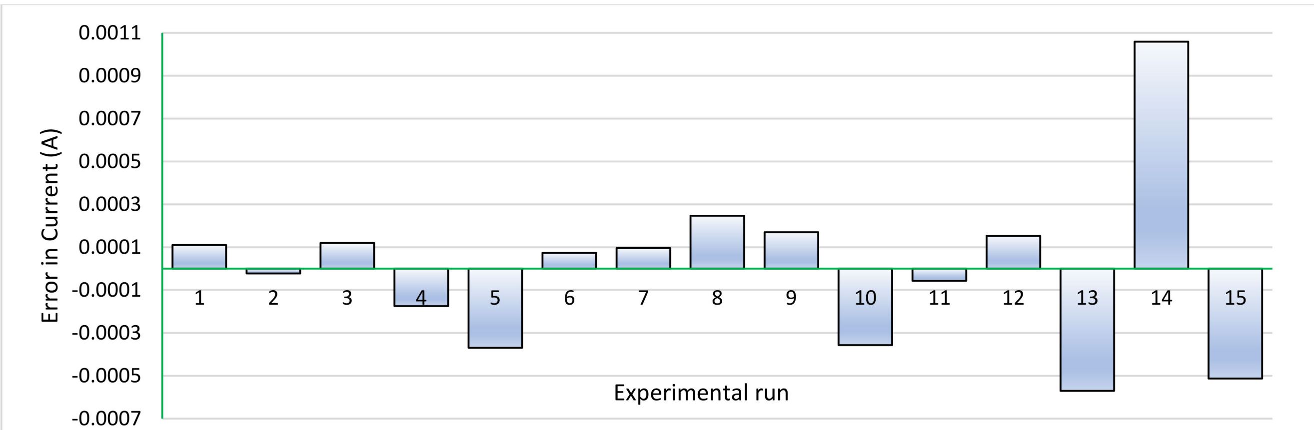

(**a**)

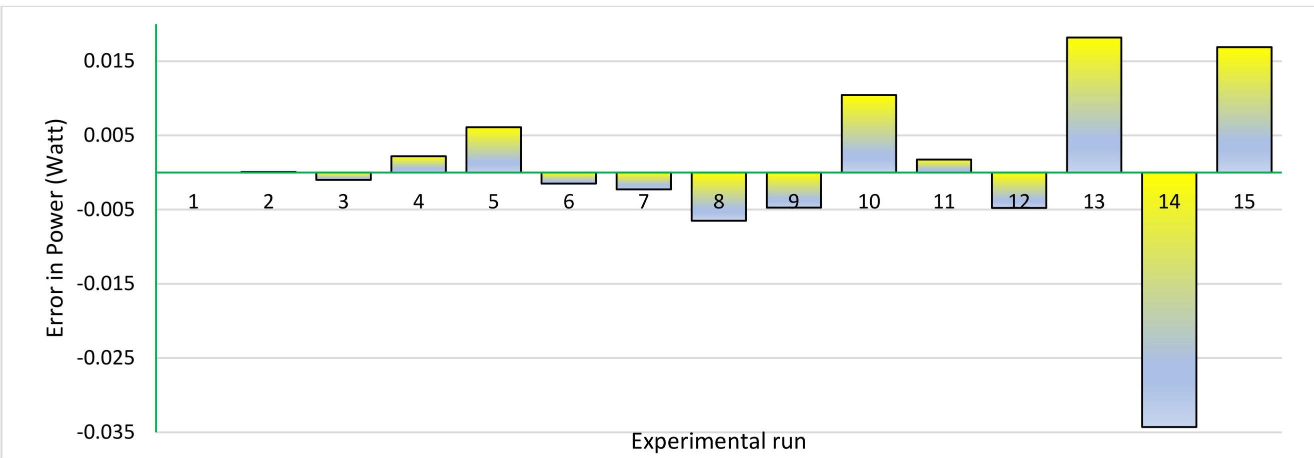

(**b**)

Figure 23. Error values for KC200GT TDM based on TFWO: (**a**) Current error values and (**b**) power error values.

Table 11. Extracted parameters for KC200GT TDM.

Algorithm	BSA	GWO	CSO	MPA	EO	BSDE	MRFO	TFWO
I_{ph} (A)	8.20173508	8.194693695	8.181855948	8.17852875	8.197397535	8.202679685	8.196629725	8.216333065
I_{s1} (A)	0.004614443	0.004525605	0.004692599	0.004752779	0.004683395	0.004733114	0.004684349	0.004855332
a_1	13.66542752	23.11163887	99.9201098	99.98707579	14.01948329	9.497022092	11.43921825	6.406246831
R_s (Ω)	3.75184×10^{-8}	8.7×10^{-9}	9.49405×10^{-8}	2.87148×10^{-7}	3.86696×10^{-8}	2.40491×10^{-7}	3.43285×10^{-7}	1.65×10^{-14}
R_{sh} (Ω)	1.238796687	1.590792134	1.481550006	1.983137731	1.238348021	1.797831823	1.89039067	1.00002872
I_{s2} (A)	1.6158×10^{-7}	6.62556×10^{-9}	1.99524×10^{-8}	3.79051×10^{-8}	7.61616×10^{-7}	3.2756×10^{-8}	3.85165×10^{-8}	2.04×10^{-9}
a2	1.775790984	1.295053844	1.213009208	1.236293271	1.991605757	1.228057245	1.238261076	1.11890891
I_{s3} (A)	4.33175×10^{-7}	7.22637×10^{-8}	1.60734×10^{-8}	1.20422×10^{-7}	2.11766×10^{-7}	1.75316×10^{-7}	7.55869×10^{-8}	3.78866×10^{-8}
a_3	1.743389601	1.284146864	1.310004248	1.967323029	1.958780659	1.917122756	1.748171665	1.270101351
RMSE	0.011035788	0.013924443	0.013060563	0.013504282	0.008423459	0.006771142	0.008878327	0.000379678

4.3.4. Statistical Analysis for KC200GT Models

For the KC200GT module, the robustness accuracy for all algorithms is evaluated for the SDM, DDM, and TDM. Table 12 records the minimum, maximum, mean, and standard deviation of the *RMSE* for the DDM. This table declares that TFWO presents the highest robustness characteristics. It gives the lowest values of the minimum, maximum, mean, and standard deviation of the *RMSE* for the three PV models.

Table 12. Statistical analysis of *RMSE* for KC200GT module with SDM, DDM, and TDM.

Model	Algorithm	*RMSE*			
		Min.	Max.	Mean	SD
SDM	TFWO	0.000636657	0.000776307	0.000643757	2.76367×10^{-5}
	MRFO	0.003374264	0.015283988	0.01143509	0.003320893
	BSDE	0.003467884	0.014320685	0.010188693	0.002289554
	MPA	0.0148696	0.048448767	0.039118106	0.010156791
	EO	0.002888472	0.01320854	0.009771334	0.002376063
	CSO	0.015480743	0.023739498	0.019620651	0.002077078
	GWO	0.023476598	0.468609138	0.164042826	0.180451636
	BSA	0.009775873	0.020577736	0.015024514	0.002330391
DDM	TFWO	0.000464919	0.003991719	0.000784157	0.000677807
	MRFO	0.008229492	0.017508428	0.013106997	0.002099435
	BSDE	0.009849963	0.029252608	0.016694172	0.004448939
	MPA	0.01025436	0.049871846	0.035790405	0.012557606
	EO	0.002599915	0.013710246	0.009972209	0.002673846
	CSO	0.004212996	0.025007328	0.017745851	0.004339108
	GWO	0.009625309	0.467884375	0.149515185	0.179605814
	BSA	0.009625725	0.026600837	0.017425267	0.003984149
TDM	TFWO	0.000379678	0.026665602	0.001706197	0.004771068
	MRFO	0.008878327	0.023401173	0.014709966	0.003787592
	BSDE	0.006771142	0.032728388	0.019233922	0.006086967
	MPA	0.013504282	0.051722136	0.039748254	0.012810733
	EO	0.008423459	0.015285328	0.011790041	0.001841909
	CSO	0.013060563	0.025146228	0.017635053	0.003334599
	GWO	0.013924443	0.4172306	0.226455866	0.174785582
	BSA	0.011035788	0.026603176	0.018267773	0.00416284

5. Conclusions

In this paper, a new application has been carried out for a new optimation algorithm called turbulent flow of water-based optimization (TFWO) for the parameter extraction of three models of PV cells. These applications are implemented on the real data of a 55 mm diameter commercial R.T.C. France solar cell and experimental data of a KC200GT module. An assessment study comparing several recent optimization techniques is employed to show the capability of the proposed TFWO algorithm. The comparative study is carried out for the same dataset and for the same computation burden. Statistical analysis is used to analyze the performance of the proposed TFWO algorithm. The high closeness between the estimated P–V and I–V curves is achieved by the proposed TFWO compared with the experimental data as well as the competitive optimization algorithms. Added to that, the proposed method has a robust performance as well as good convergence rates for all tested cases.

In future work, various environmental impacts, such as temperature, moisture, and noise, as well as the unidentifiability of parameters concept presented in [70–73], are suggested to be considered for different models as an extension of this work. Another direction is the development of solution methods with a multi-objective framework that combines the closeness of parameters and maximum benefits for power system operators.

Author Contributions: All authors have contributed to the preparation of this manuscript. M.S., A.M.S. and A.R.G. designed the strategy, studied the data, and wrote the manuscript. M.M.F.D. and K.M. revised the manuscript and investigated the optimization methodology. Finally, M.L. and R.A.E.-S. reviewed, edited, and supported different improvements to the manuscript. All authors have read and agreed to the published version of the manuscript.

Funding: This research was funded by the Department of Electrical Engineering and Automation, School of Electrical Engineering, Aalto University, Espoo, Finland.

Institutional Review Board Statement: Not applicable.

Informed Consent Statement: Not applicable.

Data Availability Statement: The data presented in this study are available on request from the corresponding author.

Conflicts of Interest: The authors declare no conflict of interest.

References

1. Afrand, M.; Shahsavar, A.; Sardari, P.T.; Sopian, K.; Salehipour, H. Energy and exergy analysis of two novel hybrid solar photovoltaic geothermal energy systems incorporating a building integrated photovoltaic thermal system and an earth air heat exchanger system. *Sol. Energy* **2019**, *188*, 83–95. [CrossRef]
2. Dong, Z.; Bingyang, L.; Qintong, Z.; Jinping, L. Thermal performance and energy characteristic analysis of multiple renewable energy complementary heat pump system. *Sol. Energy* **2020**, *196*, 287–294. [CrossRef]
3. Jurasz, J.; Canales, F.A.; Kies, A.; Guezgouz, M.; Beluco, A. A review on the complementarity of renewable energy sources: Concept, metrics, application and future research directions. *Sol. Energy* **2020**, *195*, 703–724. [CrossRef]
4. Valančius, K.; Mikučionienė, R. Solar energy as a tool of renovating soviet-type multi apartment buildings. *Sol. Energy* **2020**, *198*, 93–100. [CrossRef]
5. Herez, A.; el Hage, H.; Lemenand, T.; Ramadan, M.; Khaled, M. Review on photovoltaic/thermal hybrid solar collectors: Classifications, applications and new systems. *Sol. Energy* **2020**, *207*, 1321–1347. [CrossRef]
6. Eldin, S.A.S.; Abd-Elhady, M.S.; Kandil, H.A. Feasibility of solar tracking systems for PV panelsza in hot and cold regions. *Renew. Energy* **2016**, *85*, 228–233. [CrossRef]
7. Ahmad, L.; Khordehgah, N.; Malinauskaite, J.; Jouhara, H. Recent advances and applications of solar photovoltaics and thermal technologies. *Energy* **2020**, *207*, 118254. [CrossRef]
8. El-Negamy, M.S.; Eteiba, M.B.; El-Bayoumi, G.M. Modeling and simulation of Egyptsat-1 satellite system powered by photovoltaic module. *J. Am. Sci.* **2013**, *9*, 110–116.
9. Mahdavi, S.; Sarhaddi, F.; Hedayatizadeh, M. Energy/exergy based-evaluation of heating/cooling potential of PV/T and earth-air heat exchanger integration into a solar greenhouse. *Appl. Therm. Eng.* **2019**, *149*, 996–1007. [CrossRef]
10. Niajalili, M.; Mayeli, P.; Naghashzadegan, M.; Poshtiri, A.H. Techno-economic feasibility of off-grid solar irrigation for a rice paddy in Guilan province in Iran: A case study. *Sol. Energy* **2017**, *150*, 546–557. [CrossRef]
11. Ghasemi-Mobtaker, H.; Mostashari-Rad, F.; Saber, Z.; Chau, K.; Nabavi-Pelesaraei, A. Application of photovoltaic system to modify energy use, environmental damages and cumulative exergy demand of two irrigation systems-A case study: Barley production of Iran. *Renew. Energy* **2020**, *160*, 1316–1334. [CrossRef]
12. Zaky, A.A.; Ibrahim, M.N.; Rezk, H.; Christopoulos, E.; el Sehiemy, R.A.; Hristoforou, E.; Kladas, A.; Sergeant, P.; Falaras, P. Energy efficiency improvement of water pumping system using synchronous reluctance motor fed by perovskite solar cells. *Int. J. Energy Res.* **2020**, *44*, 11629–11642. [CrossRef]
13. Venkateswararao, A.; Ho, J.K.W.; So, S.K.; Liu, S.-W.; Wong, K.-T. Device characteristics and material developments of indoor photovoltaic devices. *Mater. Sci. Eng. R Rep.* **2020**, *139*, 100517. [CrossRef]
14. Bai, Y.; Yu, R.; Bai, Y.; Zhou, E.; Hayat, T.; Alsaedi, A.; Tan, Z. Ternary blend strategy in benzotriazole-based organic photovoltaics for indoor application. *Green Energy Environ.* **2020**. [CrossRef]
15. Ali, M.N.; Mahmoud, K.; Lehtonen, M.; Darwish, M.M.F. An Efficient Fuzzy-Logic Based Variable-Step Incremental Conductance MPPT Method for Grid-Connected PV Systems. *IEEE Access* **2021**, *9*, 26420–26430. [CrossRef]

16. Ali, M.N.; Mahmoud, K.; Lehtonen, M.; Darwish, M.M.F. Promising MPPT Methods Combining Metaheuristic, Fuzzy-Logic and ANN Techniques for Grid-Connected Photovoltaic. *Sensors* **2021**, *21*, 1244. [CrossRef] [PubMed]
17. Bayoumi, A.S.; El-Sehiemy, R.A.; Mahmoud, K.; Lehtonen, M.; Darwish, M.M.F. Assessment of an Improved Three-Diode against Modified Two-Diode Patterns of MCS Solar Cells Associated with Soft Parameter Estimation Paradigms. *Appl. Sci.* **2021**, *11*, 1055. [CrossRef]
18. Abbas, A.S.; El-Sehiemy, R.A.; Abou El-Ela, A.; Ali, E.S.; Mahmoud, K.; Lehtonen, M.; Darwish, M.M.F. Optimal Harmonic Mitigation in Distribution Systems with Inverter Based Distributed Generation. *Appl. Sci.* **2021**, *11*, 774. [CrossRef]
19. Qais, M.H.; Hasanien, H.M.; Alghuwainem, S. Transient search optimization for electrical parameters estimation of photovoltaic module based on datasheet values. *Energy Convers. Manag.* **2020**, *214*, 112904. [CrossRef]
20. Elsisi, M.; Mahmoud, K.; Lehtonen, M.; Darwish, M.M.F. An Improved Neural Network Algorithm to Efficiently Track Various Trajectories of Robot Manipulator Arms. *IEEE Access* **2021**, *9*, 11911–11920. [CrossRef]
21. Elsisi, M.; Tran, M.-Q.; Mahmoud, K.; Lehtonen, M.; Darwish, M.M.F. Deep Learning-Based Industry 4.0 and Internet of Things towards Effective Energy Management for Smart Buildings. *Sensors* **2021**, *21*, 1038. [CrossRef] [PubMed]
22. Elsisi, M.; Mahmoud, K.; Lehtonen, M.; Darwish, M.M.F. Reliable Industry 4.0 Based on Machine Learning and IoT for Analyzing, Monitoring, and Securing Smart Meters. *Sensors* **2021**, *21*, 487.
23. Mansour, D.-E.A.; Abdel-Gawad, N.M.K.; El Dein, A.Z.; Ahmed, H.M.; Darwish, M.M.F.; Lehtonen, M. Recent Advances in Polymer Nanocomposites Based on Polyethylene and Polyvinylchloride for Power Cables. *Materials* **2021**, *14*, 66. [CrossRef]
24. Abouelatta, M.A.; Ward, S.A.; Sayed, A.M.; Mahmoud, K.; Lehtonen, M.; Darwish, M.M.F. Fast Corona Discharge Assessment Using FDM integrated with Full Multigrid Method in HVDC Transmission Lines Considering Wind Impact. *IEEE Access* **2020**, *8*, 225872–225883. [CrossRef]
25. Ghoneim, S.S.M.; Mahmoud, K.; Lehtonen, M.; Darwish, M.M.F. Enhancing Diagnostic Accuracy of Transformer Faults Using Teaching-Learning Based Optimization. *IEEE Access* **2021**, 9. [CrossRef]
26. Abaza, A.; El-Sehiemy, R.A.; Mahmoud, K.; Lehtonen, M.; Darwish, M.M.F. Optimal Estimation of Proton Exchange Membrane Fuel Cells Parameter Based on Coyote Optimization Algorithm. *Appl. Sci.* **2021**, *11*, 2052. [CrossRef]
27. Lun, S.; Wang, S.; Yang, G.; Guo, T. A new explicit double-diode modeling method based on Lambert W-function for photovoltaic arrays. *Sol. Energy* **2015**, *116*, 69–82. [CrossRef]
28. Toledo, F.J.; Blanes, J.M.; Galiano, V. Two-Step Linear Least-Squares Method for Photovoltaic Single-Diode Model Parameters Extraction. *IEEE Trans. Ind. Electron.* **2018**, *65*, 6301–6308. [CrossRef]
29. Ayang, A.; Wamkeue, R.; Ouhrouche, M.; Djongyang, N.; Salomé, N.E.; Pombe, J.K.; Ekemb, G. Maximum likelihood parameters estimation of single-diode model of photovoltaic generator. *Renew. Energy* **2019**, *130*, 111–121. [CrossRef]
30. Et-Torabi, K.; Nassar-eddine, I.; Obbadi, A.; Errami, Y.; Rmaily, R.; Sahnoun, S.; El Fajri, A.; Agunaou, M. Parameters estimation of the single and double diode photovoltaic models using a Gauss–Seidel algorithm and analytical method: A comparative study. *Energy Convers. Manag.* **2017**, *148*, 1041–1054. [CrossRef]
31. Zaky, A.A.; Sehiemy, R.A.E.; Rashwan, Y.I.; Elhossieni, M.A.; Gkini, K.; Kladas, A.; Falaras, P. Optimal Performance Emulation of PSCs using the Elephant Herd Algorithm Associated with Experimental Validation. *ECS J. Solid State Sci. Technol.* **2019**, *8*, Q249–Q255. [CrossRef]
32. Yu, K.; Liang, J.J.; Qu, B.Y.; Cheng, Z.; Wang, H. Multiple learning backtracking search algorithm for estimating parameters of photovoltaic models. *Appl. Energy* **2018**, *226*, 408–422. [CrossRef]
33. Long, W.; Cai, S.; Jiao, J.; Xu, M.; Wu, T. A new hybrid algorithm based on grey wolf optimizer and cuckoo search for parameter extraction of solar photovoltaic models. *Energy Convers. Manag.* **2020**, *203*, 112243. [CrossRef]
34. Chen, H.; Jiao, S.; Heidari, A.A.; Wang, M.; Chen, X.; Zhao, X. An opposition-based sine cosine approach with local search for parameter estimation of photovoltaic models. *Energy Convers. Manag.* **2019**, *195*, 927–942. [CrossRef]
35. Jian, X.; Weng, Z. A logistic chaotic JAYA algorithm for parameters identification of photovoltaic cell and module models. *Optik* **2020**, *203*, 164041. [CrossRef]
36. Zhang, H.; Heidari, A.A.; Wang, M.; Zhang, L.; Chen, H.; Li, C. Orthogonal Nelder-Mead moth flame method for parameters identification of photovoltaic modules. *Energy Convers. Manag.* **2020**, *211*, 112764. [CrossRef]
37. Li, S.; Gong, W.; Yan, X.; Hu, C.; Bai, D.; Wang, L.; Gao, L. Parameter extraction of photovoltaic models using an improved teaching-learning-based optimization. *Energy Convers. Manag.* **2019**, *186*, 293–305. [CrossRef]
38. Allam, D.; Yousri, D.A.; Eteiba, M.B. Parameters extraction of the three diode model for the multi-crystalline solar cell/module using Moth-Flame Optimization Algorithm. *Energy Convers. Manag.* **2016**, *123*, 535–548. [CrossRef]
39. Chenouard, R.; El-Sehiemy, R.A. An interval branch and bound global optimization algorithm for parameter estimation of three photovoltaic models. *Energy Convers. Manag.* **2020**, *205*, 112400. [CrossRef]
40. Niu, Q.; Zhang, H.; Li, K. An improved TLBO with elite strategy for parameters identification of PEM fuel cell and solar cell models. *Int. J. Hydrog. Energy* **2014**, *39*, 3837–3854. [CrossRef]
41. Elaziz, M.A.; Oliva, D. Parameter estimation of solar cells diode models by an improved opposition-based whale optimization algorithm. *Energy Convers. Manag.* **2018**, *171*, 1843–1859. [CrossRef]
42. Oliva, D.; Ewees, A.A.; Aziz, M.A.E.; Hassanien, A.E.; Peréz-Cisneros, M. A Chaotic Improved Artificial Bee Colony for Parameter Estimation of Photovoltaic Cells. *Energies* **2017**, *10*, 865. [CrossRef]

43. Shaheen, A.M.; Ginidi, A.R.; El-Sehiemy, R.A.; Ghoneim, S.S.M. A Forensic-Based Investigation Algorithm for Parameter Extraction of Solar Cell Models. *IEEE Access* **2021**, *9*, 1–20. [CrossRef]
44. Ismaeel, A.A.K.; Houssein, E.H.; Oliva, D.; Said, M. Gradient-based optimizer for parameter extraction in photovoltaic models. *IEEE Access* **2021**, *9*, 13403–13416. [CrossRef]
45. Ghasemi, M.; Davoudkhani, I.F.; Akbari, E.; Rahimnejad, A.; Ghavidel, S.; Li, L. A novel and effective optimization algorithm for global optimization and its engineering applications: Turbulent Flow of Water-based Optimization (TFWO). *Eng. Appl. Artif. Intell.* **2020**, *92*, 103666. [CrossRef]
46. García, R.M.A.; Abril, I.P. Photovoltaic module model determination by using the Tellegen's theorem. *Renew. Energy* **2020**, *152*, 409–420. [CrossRef]
47. Civicioglu, P. Backtracking Search Optimization Algorithm for numerical optimization problems. *Appl. Math. Comput.* **2013**, *219*, 8121–8144. [CrossRef]
48. Mirjalili, S.; Mirjalili, S.M.; Lewis, A. Grey wolf optimizer. *Adv. Eng. Softw.* **2014**, *69*, 46–61. [CrossRef]
49. Askarzadeh, A. A novel metaheuristic method for solving constrained engineering optimization problems: Crow search algorithm. *Comput. Struct.* **2016**, *169*, 1–12. [CrossRef]
50. Faramarzi, A.; Heidarinejad, M.; Stephens, B.; Mirjalili, S. Equilibrium optimizer: A novel optimization algorithm. *Knowl. Based Syst.* **2020**, *191*, 105190. [CrossRef]
51. Faramarzi, A.; Heidarinejad, M.; Mirjalili, S.; Gandomi, A.H. Marine Predators Algorithm: A nature-inspired metaheuristic. *Expert Syst. Appl.* **2020**, *152*, 113377. [CrossRef]
52. Bernstein-Levy Search Differential Evolution Algorithm. Available online: https://www.mathworks.com/matlabcentral/fileexchange/77374-bernstein-levy-search-differential-evolution-algorithm (accessed on 1 March 2021).
53. Zhao, W.; Zhang, Z.; Wang, L. Manta ray foraging optimization: An effective bio-inspired optimizer for engineering applications. *Eng. Appl. Artif. Intell.* **2020**, *87*, 103300. [CrossRef]
54. Shaheen, A.M.; El-Sehiemy, R.A. Enhanced feeder reconfiguration in primary distribution networks using backtracking search technique. *Aust. J. Electr. Electron. Eng.* **2020**, *17*, 1–7. [CrossRef]
55. Shaheen, A.M.; el Sehiemy, R.A.; Farrag, S.M. Integrated Strategies of Backtracking Search Optimizer for Solving Reactive Power Dispatch Problem. *IEEE Syst. J.* **2018**, 12. [CrossRef]
56. Tian, Z. Backtracking search optimization algorithm-based least square support vector machine and its applications. *Eng. Appl. Artif. Intell.* **2020**, *94*, 103801. [CrossRef]
57. Abou-El-Ela, A.; L-Sehiemy, R.E.; Shaheen, A.M.; Eissa, I. Optimal coordination of static VAR compensators, fixed capacitors, and distributed energy resources in Egyptian distribution networks. *Int. Trans. Electr. Energy Syst.* **2020**. [CrossRef]
58. Shaheen, A.M.; el Sehiemy, R. Optimal co-ordinated allocation of distributed generation units/capacitor banks/voltage regulators by EGWA. *IEEE Syst. J.* **2020**. [CrossRef]
59. El-Bidairi, K.S.; Nguyen, H.D.; Jayasinghe, S.D.G.; Mahmoud, T.S.; Penesis, I. A hybrid energy management and battery size optimization for standalone microgrids: A case study for Flinders Island, Australia. *Energy Convers. Manag.* **2018**, *175*, 192–212. [CrossRef]
60. Memarzadeh, G.; Keynia, F. A new short-term wind speed forecasting method based on fine-tuned LSTM neural network and optimal input sets. *Energy Convers. Manag.* **2020**, *213*, 112824. [CrossRef]
61. Shaheen, A.M.; El-Sehiemy, R.A. Optimal allocation of capacitor devices on MV distribution networks using crow search algorithm. In Proceedings of the 24th International Conference on Electricity Distribution, Glasgow, Scotland, 12–15 June 2017. Paper No. 20.
62. El Ela, A.A.A.; El-Sehiemy, R.A.; Shaheen, A.M.; Shalaby, A.S. Application of the crow search algorithm for economic environmental dispatch. In Proceedings of the 2017 Nineteenth International Middle East Power Systems Conference (MEPCON), Cairo, Egypt, 19–21 December 2017.
63. Abdel-Basset, M.; Chang, V.; Mohamed, R. A novel equilibrium optimization algorithm for multi-thresholding image segmentation problems. *Neural Comput. Appl.* **2020**. [CrossRef]
64. Abdul-Hamied, D.T.; Shaheen, A.M.; Salem, W.A.; Gabr, W.I.; El-Sehiemy, R.A. Equilibrium optimizer based multi dimensions operation of hybrid AC/DC grids. *Alex. Eng. J.* **2020**, *59*, 4787–4803. [CrossRef]
65. Yousri, D.; Babu, T.S.; Beshr, E.; Eteiba, M.B.; Allam, D. A Robust Strategy Based on Marine Predators Algorithm for Large Scale Photovoltaic Array Reconfiguration to Mitigate the Partial Shading Effect on the Performance of PV System. *IEEE Access* **2020**, *8*, 112407–112426. [CrossRef]
66. Abdel-Basset, M.; Mohamed, R.; Elhoseny, M.; Bashir, A.K.; Jolfaei, A.; Kumar, N. Energy-Aware Marine Predators Algorithm for Task Scheduling in IoT-based Fog Computing Applications. *IEEE Trans. Ind. Inf.* **2020**, 1. [CrossRef]
67. Xu, H.; Song, H.; Xu, C.; Wu, X.; Yousefi, N. Exergy analysis and optimization of a HT-PEMFC using developed Manta Ray Foraging Optimization Algorithm. *Int. J. Hydrog. Energy* **2020**, *45*, 30932–30941. [CrossRef]
68. Elattar, E.E.; Shaheen, A.M.; Elsayed, A.M.; El-Sehiemy, R.A. Optimal Power Flow with Emerged Technologies of Voltage Source Converter Stations in Meshed Power Systems. *IEEE Access* **2020**, *8*, 166963–166979. [CrossRef]
69. Fathy, A.; Rezk, H.; Yousri, D. A robust global MPPT to mitigate partial shading of triple-junction solar cell-based system using manta ray foraging optimization algorithm. *Sol. Energy* **2020**, *207*, 305–316. [CrossRef]

70. Kiparissides, A.; Koutinas, M.; Kontoravdi, C.; Mantalaris, A.; Pistikopoulos, E.N. 'Closing the loop' in biological systems modeling—From the in silico to the in vitro. *Automatica* **2011**, *47*, 1147–1155. [CrossRef]
71. Kravaris, C.; Hahn, J.; Chu, Y. Advances and selected recent developments in state and parameter estimation. *Comput. Chem. Eng.* **2013**, *51*, 111–123. [CrossRef]
72. Villaverde, A.F.; Barreiro, A.; Papachristodoulou, A. Structural Identifiability of Dynamic Systems Biology Models. *PLoS Comput. Biol.* **2016**, *12*, e1005153. [CrossRef]
73. Bendary, A.F.; Abdelaziz, A.Y.; Ismail, M.M.; Mahmoud, K.; Lehtonen, M.; Darwish, M.M.F. Proposed ANFIS Based Approach for Fault Tracking, Detection, Clearing and Rearrangement for Photovoltaic System. *Sensors* **2021**, *21*, 2269. [CrossRef]